EVALUATION OF STRESS CORROSION CRACKING IN SENSITIZED 304 STAINLESS STEEL USING NONLINEAR RAYLEIGH WAVES

A Thesis
Presented to
The Academic Faculty

by

Florian Morlock

In Partial Fulfillment
of the Requirements for the Degree
Master of Science in
Engineering Science and Mechanics

School of Civil and Environmental Engineering
Georgia Institute of Technology
December 2014

Copyright ©2014 Florian Morlock

EVALUATION OF STRESS CORROSION CRACKING IN SENSITIZED 304 STAINLESS STEEL USING NONLINEAR RAYLEIGH WAVES

Approved by:

Professor Laurence J. Jacobs, Advisor
School of Civil and Environmental Engineering
Georgia Institute of Technology

Dr. Jin-Yeon Kim
School of Civil and Environmental Engineering
Georgia Institute of Technology

Dr. Jianmin Qu
Department of Civil and Environmental Engineering
Northwestern University

Date Approved: August 22 2014

ACKNOWLEDGEMENTS

In the first place, I want to thank my advisor during this research Prof. Laurence J. Jacobs. He supported me and gave me motivation when it was necessary throughout my stay in Atlanta. In particular, I want to thank him for giving me the opportunity to come to Georgia Tech to write this thesis and to present its results at the 2014 QNDE Conference in Boise, Idaho. I also want to thank Dr. Jin-Yeon Kim for giving me advice in the field of wave propagation and Rayleigh wave measurements. Furthermore I want to thank Dr. Jianmin Qu from the Northwestern University for reviewing my thesis and serving as a committee member.

A special thank goes to Prof. Preet M. Singh from the School of Material Science and Engineering at Georgia Tech for giving me valuable insights considering the topic of material science, in particular the issue of stress corrosion cracking. In addition to that I want to thank Prof. Singh for allowing and helping me to use his equipment.

Furthermore, I would like to thank Prof. Lothar Gaul and Christian Ehrlich from the Institute of Applied and Experimental Mechanics at the University of Stuttgart for organizing this program together with Prof. Jacobs, advising me during the preparation of my year abroad and initially choosing me as a candidate for this program. Associated with that, I want to acknowledge the German Academic Exchange Service (DAAD) for financially supporting me.

Further thank goes to my labmates Katie Matlack, Anne Romer, Daniel Marino, David Torello and Gun Kim. Particularly, I want to thank Anne Romer and Daniel Marino for sharing joy and sorrow with me during this year in Atlanta.

Finally I want to thank all my friends and family back in Germany for their support.

TABLE OF CONTENTS

LIST OF TABLES

LIST OF FIGURES

LIST OF SYMBOLS

Symbol	Description
A, B	amplitudes
A_1	amplitude of the fundamental frequency
A_2	amplitude of the second harmonic
c	wave speed
C_{ijkl}	second order elastic modulus
C_{ijklmn}	third order elastic modulus
c_L, c_S, c_R	longitudinal, shear and Rayleigh wave speed
C	constant
$\mathbf{d}$	unit particle motion vector
E	Young's modulus
$\mathbf{E}$	Lagrangian strain tensor
f	frequency
f_i	body forces
$\mathbf{F}$	deformation gradient tensor
i	imaginary unit
k	wavenumber
M_{ijklmn}	Combination of second and third order moduli
n_i	normal vector
O	higher order terms
p	wave speed depending constant
$\mathbf{p}$	unit propagation direction vector
$\mathbf{P}$	Piola-Kirchhoff stress tensor
s	wave speed depending constant
S	surface

Symbol	Description
t_i	surface traction
$\mathbf{u}$	displacement vector
V	volume
W	specific strain energy per unit mass
x	propagation distance
$\mathbf{x}$	position vector
$\mathbf{x}^*$	Lagrangian particle coordinate
β	nonlinearity parameter
β'	relative nonlinearity parameter
δ_{ij}	Kronecker delta
$\boldsymbol{\epsilon}$ or ϵ_{ij}	strain tensor
Θ	angle of incident / reflected / transmitted wave
λ	wavelength
λ, μ	Lamé constants
ν	Poisson's ratio
ρ	density
$\boldsymbol{\sigma}$ or σ_{ij}	stress tensor
φ, θ	displacement potentials
ω	angular frequency
∇	Nabla operator

SUMMARY

This research uses nonlinear Rayleigh surface waves to characterize stress corrosion cracking (SCC) damage in sensitized 304 Stainless Steel (304 SS). 304 SS is widely used in reactor pressure vessels and fuel pipelines, where a corrosive environment in combination with applied stress due to high internal pressures can cause SCC. SCC poses great risk to these structures as it initiates cracks late in the lifetime and often unexpectedly. The initiated microcracks grow and accumulate very quickly to form macroscopic cracks that lead to material failure. Welds and the nearby heat affected zones (HAZ) in the vessels and pipework are particularly affected by SCC as welding induces sensitization in the material. SCC damage results in microstructural changes such as dislocation movement and microcrack initiation that in the long term lead to reduced structural integrity and material failure. Therefore, the early detection of SCC is crucial to ensure safe operation. It has been shown that the microstructural changes caused by SCC can generate higher harmonic waves when excited harmonically. This research considers different levels of SCC damage induced in samples of sensitized 304 SS by applying stress to a specimen held in a corrosive medium (Sodium Thiosulfate). Nonlinear Rayleigh surface waves are introduced in the material and the fundamental and the second harmonic waves are measured. The nonlinearity parameter that relates the fundamental and the second harmonic amplitudes, is computed to quantify the SCC damage in each sample. The results obtained are used to demonstrate the feasibility of using nonlinear Rayleigh waves to characterize SCC damage.

CHAPTER I

INTRODUCTION

1.1 Motivation and Objectives

This research uses nonlinear ultrasound to investigate the stress corrosion cracking behavior of type 304 stainless steel (304 SS), a versatile and widely used austenitic stainless steel. Austenitic stainless steels are iron-based alloys with high chromium ($\approx$ 19%) and nickel ($\approx$ 9%), content which make these type of steel resistant to corrosion in a wide range of atmospheric environments and corrosive media. As the name implies, the predominant microstructural phase in austenitic stainless steels at room temperature is austenite. Type 304 stainless steel owes its usage in a wide range of applications, amongst other properties, to its forming and welding characteristics. Besides its use for kitchen equipment and architectural moldings and trim, 304 stainless steel is widely used for welded components in the the textile, paper, pharmaceutical and chemical industry, including fuel pipelines. Of high interest is 304 SS application in welded fuel pipelines and reactor pressure vessels which can involve the issue of stress corrosion cracking (SCC) [16]. Welding provokes microstructural changes in the heat affected zone (HAZ) of the weld, that make the material susceptible to SCC. This process is called sensitization of austenitic stainless steels and this phenomena will be examined in detail in this thesis. The induced SCC, in turn, can pose great risk to these structural components as it is deemed an "insidious" process that can arise unexpectedly [21]. Microcracks due to SCC can be initiated rather late in the lifetime of a structural component and grow very fast once initiated [25]. As microcracks grow larger and join together, they become macrocracks that can lead to structural failure. Macrocracks can be detected by a wide range of linear ultrasonic

techniques. Unfortunately, these linear ultrasonic techniques are not capable of detecting the microstructural precursors in a material, such as changes in dislocation density and precipitates. On the other hand, nonlinear ultrasonic methods are sensitive to these microstructural changes and have the potential to be detect changes in in the lifetime of a SCC loaded component.

Once initiated, stress corrosion cracks can quickly grow into macroscopic cracks that lead to component failure. Therefore, it is important to detect SCC in a material as soon as possible. Here, nonlinear ultrasonic techniques can potentially detect SCC before macrocracks are formed. Amongst other types of propagating waves, Rayleigh surface waves have many advantages for detecting SCC damage, since the energy of a Rayleigh wave is concentrated near the surface where microcrack growth is initiated. The objective of this research is to develop a robust method to characterize SCC in 304 SS using nonlinear Rayleigh surface waves. The goal is to use nonlinear Rayleigh wave measurements to quantify the level of SCC damage induced in a specimen. 304 SS samples with different levels of induced SCC damage are produced, and then tracked with nonlinear Rayleigh waves. This research examines two different detection methods – an air-coupled receiver and wedge detection – to measure the increase in acoustic nonlinearity as a function of propagation distance. Finally, a complementary microscopic analysis of these samples is used to track the level of SCC damage in each specimen and to help interpret the results from the nonlinear ultrasonic measurements.

1.2 Structure of Thesis

Chapter (2) covers the mathematical background of this research and the fundamentals of wave propagation. After discussing the fundamentals of wave propagation, the

characteristics of Rayleigh waves are derived by means of wave reflection and transmission. Furthermore, the fundamentals of nonlinear wave propagation and the effect of material nonlinearity on a propagating Rayleigh wave are introduced, including the relative nonlinearity parameter β'.

In chapter (3), the issue of stress corrosion cracking is discussed. This chapter emphasizes the threat SCC involves and briefly describes the process of stress corrosion cracking itself. Furthermore, the impact of sensitization and its similarities regarding the microstructural changes due to welding processes are discussed. Lastly, the possible microstructural changes occurring during sensitization and SCC are related to an expected change in the relative nonlinearity parameter.

Chapter (4) discuss the fabrication of the samples used in this research in detail. As nonlinear ultrasonic methods are very sensitive to microstructural changes in the material, particular attention is given to the fabrication and preconditioning processes. Also some basic thoughts on measurements on actual welded samples and the informative value of measurements on sensitized samples are presented in terms of the issue of SCC in welded 304 SS components. However, the focal point of this chapter is the introduction of SCC in the samples including the issue of sensitization and the SCC setup itself.

The experimental setup with all its components is presented in chapter (5). In this chapter, the advantage of varying the propagation distance to extract the cumulative noninearity is discussed. Then two methods for the detection of the propagating Rayleigh waves are presented – air-coupled and wedge detection.

Chapter (6) presents preliminary results of this research. A comparison between air-coupled and wedge detection is drawn to decide on a robust method providing satisfying results. Additionally, measurements on a welded 304 SS plate are presented to underline the issue with welding regions.

In chapter (7) the feasibility of tracking SCC damage with nonlinear Rayleigh wave

measurements is shown. This chapter discusses the results obtained to the extent of this research and relates changes in measured material nonlinearity to microstructural changes due to sensitization and SCC damage. It also provides microscopic images of the sample surfaces to underline the nonlinear ultrasonic measurements.

Lastly, chapter (8) is a conclusion and an outlook for possible future research based on the results of this work.

CHAPTER II

WAVE PROPAGATION

This chapter discusses wave propagation in elastic solids. Firstly, the basic equations of motion are derived. Later in this chapter, some concepts of linear and nonlinear wave propagation are discussed

2.1 Equation of Motion

As a starting point, we use the most general form of the balance of linear momentum which is, according to Aschenbach [2], given by the expression

$$\int_S t_i \mathrm{d}S + \int_V \rho f_i \mathrm{d}V = \int_V \rho \ddot{u}_i \mathrm{d}V \tag{2.1}$$

Here, S and V are the surface and volume of a closed region of a body, whereas, t_i and f_i depict the surface traction and the body force it is exposed to. Using the Cauchy stress definition we can substitute

$$t_i = \sigma_{ki} n_k \tag{2.2}$$

into (2.1). Here, n_k is the surface's normal vector component in k-direction. To transform the surface integral into a volume integral, we apply the Gauss' theorem

$$\iint_S F_i n_i \mathrm{d}S = \iiint_V \frac{\partial F_i}{\partial x_i} \mathrm{d}V \tag{2.3}$$

to obtain the volume integral form

$$\int_V (\sigma_{ij,j}) \mathrm{d}V + \int_V (\rho f_i) \mathrm{d}V = \int_V (\rho \ddot{u}_i) \mathrm{d}V. \tag{2.4}$$

This equation must hold for arbitrary V. Therefore, we can factor out the integration to obtain Cauchy's first law of motion

$$\sigma_{ij,j} + \rho f_i = \rho \ddot{u}_i. \tag{2.5}$$

By using constitutive stress-strain relations, we can substitute the Cauchy stress σ_{ij} to obtain an equation that is only dependent on the displacement $\mathbf{u}$. For the general linear elastic case, the stress σ_{ij} and the strain ϵ_{kl} can be related using the fourth order elastic stiffness tensor C_{ijkl} by

$$\sigma_{ij} = C_{ijkl}\epsilon_{kl}. \tag{2.6}$$

This fourth order elastic stiffness tensor generally consists of $3^4 = 81$ components. However, for different assumptions these components become dependent from each other which simplifies the stress-strain relationship. Regarding an isotropic and homogeneous material, the elastic stiffness tensor can be characterized by two independent constants, e.g. the Lamé constants λ and μ defined by

$$\lambda = \frac{E\nu}{(1+\nu)(1-2\nu)} \tag{2.7}$$

and

$$\mu = \frac{E}{2(1+\nu)} \tag{2.8}$$

with the material constants Young's modulus E and Poisson's ratio ν. This simplifies the stress-strain relationship to

$$\sigma_{ij} = \lambda\epsilon_{kk}\delta_{ij} + 2\mu\epsilon_{ij}. \tag{2.9}$$

Moreover, the strain $\boldsymbol{\epsilon}$ can, then, be defined in terms of displacement $\mathbf{u}$ by

$$\epsilon_{ij} = \frac{1}{2}(u_{i,j} + u_{j,i}). \tag{2.10}$$

By substituting all this into Cauchy's first law of motion (2.5) and neglecting body forces f_i we obtain Navier's equation of motion, which is a differential equation solely depending on the displacement $\mathbf{u}$

$$(\lambda + \mu)u_{j,ji} + \mu u_{i,ji} = \rho\ddot{u}_i. \tag{2.11}$$

Using vectorial instead of Einstein notation, we can rewrite this equation as

$$\mu\nabla^2\mathbf{u} + (\lambda+\mu)\nabla\nabla\cdot\mathbf{u} = \rho\ddot{\mathbf{u}}. \tag{2.12}$$

For the general case of a wave propagating in all three dimensions of a body, equations (2.11) and (2.12) describe three coupled partial differential equations depending on material properties and displacement $\mathbf{u}$ only. A solution for these differential equations can be found by introducing a scalar potential φ and a vector potential ψ. Using these potentials, a solution for $\mathbf{u}$ can be expressed in the form

$$\mathbf{u} = \nabla\varphi + \nabla\times\psi. \tag{2.13}$$

By using mathematical principles on potentials and substituting (2.13) into (2.12) with the additional constraint on the vector potetial

$$\nabla\cdot\psi = 0 \tag{2.14}$$

we can split up the Navier's equation into uncoupled differential equations in terms of the scalar potential φ and the vector potential ψ

$$(\lambda+2\mu)\nabla^2\varphi = \rho\ddot{\varphi} \tag{2.15}$$

$$\mu\nabla\psi = \rho\ddot{\psi}, \tag{2.16}$$

Introducing the definitions of the longitudinal and the shear wave velocities c_L and c_S

$$c_L = \sqrt{\frac{\lambda+2\mu}{\rho}} \tag{2.17}$$

$$c_S = \sqrt{\frac{\mu}{\rho}} \tag{2.18}$$

we can rewrite (2.15) and (2.16) as

$$\nabla^2\varphi = \frac{1}{c_L^2}\ddot{\varphi} \tag{2.19}$$

$$\nabla^2\psi = \frac{1}{c_S^2}\ddot{\psi}. \tag{2.20}$$

Equations (2.19) and (2.20) finally give us the equations of motion for a longitudinal and a shear wave propagating in a linear-elastic, isotropic and homogeneous solid.

2.2 Linear Wave Propagation

2.2.1 Plane Waves

A plane wave is a wave of constant frequency whose wavefronts are infinite parallel planes. This implies that the displacement $\mathbf{u}$, strain $\boldsymbol{\epsilon}$ and the stress $\boldsymbol{\sigma}$ adopt a constant value on each of these parallel planes. The normalized vector perpendicular to the wavefreont-planes is called the unit propagation verctor $\mathbf{p}$.

Regarding a point source emitting a three-dimensional wave, as in the example of a drop in the water we can assume parallel wavefronts (painted in dashed green lines) when the distance to the source is relatively large, compared to its wavelength λ (see figure (2.2.1)). In this, so called far field of a propagating wave, the wave can be assumed as a plane wave.

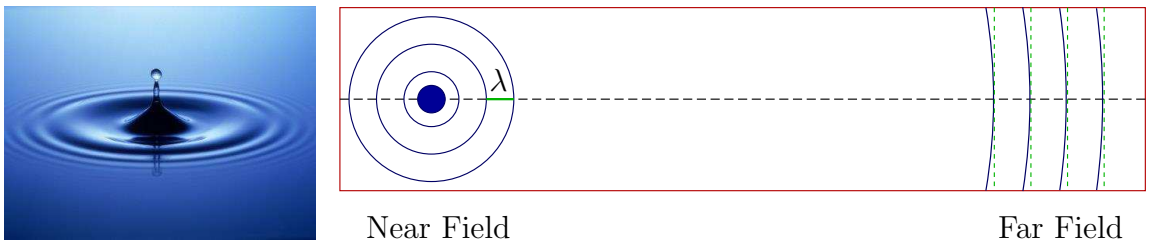

Figure 2.1: water drop [9] (left) and its Near and Far Field (right)

For the following considerations we will regard a plane wave propagating through an isotropic and homogeneous elastic solid. Under these assumptions, the displacement vector $\mathbf{u}$ can be expressed using the unit propagation verctor $\mathbf{p}$ and the unit particle motion vector $\mathbf{d}$ by

$$\mathbf{u} = f(\mathbf{x} \cdot \mathbf{p} - ct)\mathbf{d}. \tag{2.21}$$

As already stated, the unit propagation vector points in directions perpendicular to the wavefronts. The unit particle motion vector $\mathbf{d}$ is a normalized vector pointing in the direction along which a single particle is displaced. In this equation c can be both, the longitudinal wave velocity c_L or the shear wave velocity c_S. Substituting (2.21) into Navier's equation of motion (2.12) while still neglecting body forces f_i, we obtain

$$(\mu - \rho c^2)\mathbf{d} + (\lambda + \mu)(\mathbf{p} \cdot \mathbf{d})\mathbf{p} = 0. \tag{2.22}$$

This equation cannot be satisfied for arbitrary propagation and particle displacement vectors $\mathbf{p}$ and $\mathbf{d}$, but only for perpendicular or parallel $\mathbf{p}$ and $\mathbf{d}$. Thus, there are two solutions for the Navier's equation for plane waves:

In the first case, $\mathbf{p}$ and $\mathbf{d}$ are parallel, so $\mathbf{p} = \pm\mathbf{d}$ and $\mathbf{p} \cdot \mathbf{d} = \pm 1$. In this case, we consider a longitudinal wave or P-wave, where the wave propagates in the same direction as the particle movement. Solving equation (2.22) for the velocity c we obtain the longitudinal wave speed

$$c = c_L = \sqrt{\frac{\lambda + 2\mu}{\rho}}. \tag{2.23}$$

In the second case, $\mathbf{p}$ and $\mathbf{d}$ are perpendicular, so $\mathbf{p} \cdot \mathbf{d} = 0$. Here, we consider a shear wave or S-wave, where the propagation direction of the wave is perpendicular to the particle motion. Solving the Navier's equation (2.22) for the wave velocity c gives us the shear wave speed

$$c = c_S = \sqrt{\frac{\mu}{\rho}}. \tag{2.24}$$

A first conclusion that can be drawn from the two equations (2.23) and (2.24) is that the $c_L > c_S$ is true for all elastic solids. This means that longitudinal waves propagate faster than shear waves.

Moreover, we can define the wavenumber k of a wave with

$$k = \frac{\omega}{c} \tag{2.25}$$

where ω is the frequency of the wave and c is the speed at which the wave propagates.

2.2.2 Plane Wave reflection at a Stress Free Surface

The displacement field of a harmonic plane wave propagating in the x_1,x_2-plane can also be written using complex notation as presented in [2]

$$\mathbf{u}^{(n)} = A_n \mathbf{d}^{(n)} \exp\left[\mathrm{i}k_n\left(x_1 p_1^{(n)} + x_2 p_2^{(n)} - c_n t\right)\right]. \tag{2.26}$$

Here, the index n distinguishs between a longitudinal (P-wave) and a vertically polarized shear wave (SV-wave) propagating in the (x_1,x_2)-plane. Vertically polarized implies that the particle movement is in the (x_1,x_2)-plane but not in x_3-direction. Similarly, there are horizontally polarized shear waves (SH-waves), where the particle movement is in the (x_1, x_3)-plane but not in x_2-direction. A_n denotes the amplitude of the propagating wave.

In the most general case of a surface forming a boundary between two solid media, any incident wave (P- or SV-wave) will cause reflected as well as transmitted P- and SV-waves. The transmitted and reflected displacement fields can be evaluated using boundary conditions for this incident.

In the case of a stress free boundary, we assume the second medium to be vacuum, so it does not raise any force on the first medium. This implies that there is no transmission, but only reflection such that the whole energy stays in the medium. Any incident P- or SV-wave will therefore cause two reflected waves, but no transmitted one. Figure (2.2) shows the reflected waves of an incident P- or SV-wave propagating towards the stress free surface under the angle θ_0.

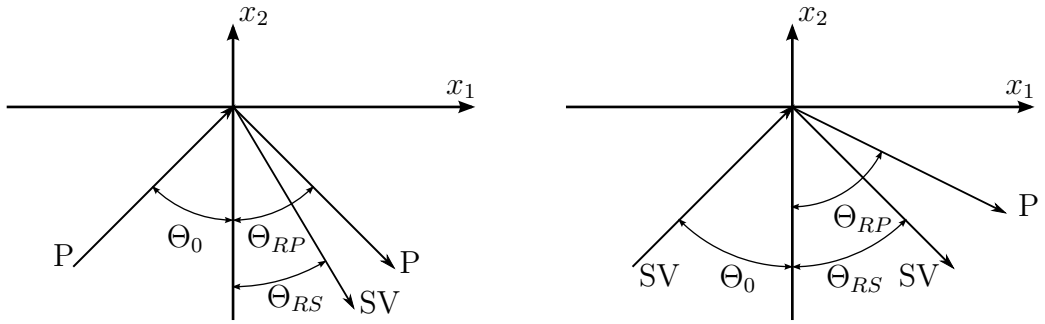

Figure 2.2: Reflection of an initial P- or SV-wave on a stress free boundary

The boundary conditions for the reflection at a stress free surface propagating in the displayed (x_1,x_2)-plane are $\sigma_{22} = 0$ and $\sigma_{12} = 0$ at $x_2 = 0$.
According to Snell's law, the angles of the incident and reflected waves are related by

$$k_n \sin\theta_0 = k_P \sin\theta_{RP} = k_S \sin\theta_{RS}. \tag{2.27}$$

Again, n denotes if the incident wave is a P- or a SV-wave. Equation (2.27) yields the angular relationships denoted in table (2.1), depending on the incident wave.

Table 2.1: Angles of incident and reflected waves

Incident wave with angle θ_0	θ_{RP}	θ_{RS}
P (incident)	$\theta_{RP} = \theta_0$	$\theta_{RS} = \frac{c_S}{c_L} \sin\theta_0$
SV (incident)	$\theta_{RP} = \frac{c_L}{c_S} \sin\theta_0$	$\theta_{RS} = \theta_0$

However, there are two special cases for the reflection on a stress free boundary:

1. First, if $\theta_0 = 0$ the incident wave (P- or SV-wave) hits the stress free boundary orthogonal. In this case, there will be only one reflected wave. The reflected wave will be exactly the same as the incident wave.

2. Seond, for an incident SV-wave there exists a critical incident angle θ_c. If $\theta_0 > \theta_c$ there will be a reflected SV-wave only. The reflected P-wave portion will propagate in the form of a surface wave, e.g. a Rayleigh surface wave, which will be

discussed later in this chapter and will be used for the nondestructive evaluation in this research. The critical angle for this case is defined by Snell's Law as $\theta_c = \arcsin \frac{c_S}{c_L}$.

2.3 Rayleigh Surface Waves

Rayleigh waves are surface acoustic waves (SAWs) that travel along a stress free boundary of a solid. SAWs have the attribute to decay exponentially with depth which results in an energy concentration near the surface. According to Rose [20], Rayleigh waves find particular application in ultrasonic nondestructive evaluation (NDE).

In Graff [10], the motion of a particle excited by a Rayleigh wave is described as an elliptical loop. Its track can be split up into a superposition of a longitudinal and a shear displacement. Figure (2.3) shows the displacement field of a two-dimensional rayleigh wave propagating in x_1-direction. Additionally, it shows the elliptical path of an isolated particle and the amplitude of the displacement u_x in x-direction as a funtion of depth (z).

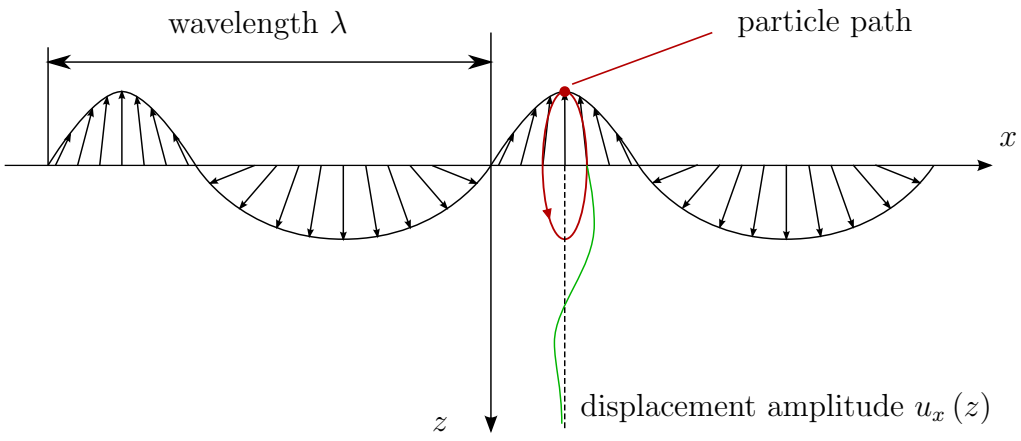

Figure 2.3: Displacement field of a two-dimensional Rayleigh wave propagating in x-direction

A good approach to start defining the displacement field of a Rayleigh wave mathematically is the use of the earlier mentioned potentials φ and ψ. According to Viktorov [23], in the case of a two-dimensional plane wave propagating in positive x direction with the z-axis normal to the surface, pointing into the solid, the potentials of a Rayleigh surface wave can be assumed as

$$\varphi = -i\frac{B_1}{k_R}e^{-pz}e^{i(k_R x-\omega t)} \tag{2.28}$$

$$\psi = -i\frac{C}{k_R}e^{-sz}e^{i(k_R x-\omega t)} \tag{2.29}$$

Here, B_1 and C are the amplitudes of displacement in x and z direction, k_R and c_R are the wavenumber and phase velocity of the Rayleigh wave and the parameters p and s are defined by

$$p^2 = k_R^2 - k_L^2 \tag{2.30}$$

$$s^2 = k_R^2 - k_S^2, \tag{2.31}$$

where k_L and k_S are the wavenumbers of longitudinal and shear waves in the medium. By applying stress free boundary conditions and substituting (2.28) and (2.29) into the wave equations equations (2.19) and (2.20) we can relate the two amplitudes B_1 and C with the wavenumber k_R

$$B_1 = -i\frac{2k_R p}{k_R^2 + s^2}C. \tag{2.32}$$

Furthermore, this relation can be used to establish a characteristic equation to determine the Rayleigh wave speed c_R

$$\left(2 - \frac{c_R^2}{c_S^2}\right)^2 - 4\left(1 - \frac{c_R^2}{c_L^2}\right)^{\frac{1}{2}}\left(1 - \frac{c_R^2}{c_S^2}\right)^{\frac{1}{2}}. \tag{2.33}$$

Using a simple transformation, this characteristic equation can be simplified to the well known Rayleigh equation

$$\eta^6 - 8\eta^4 + 8\left(3 - 2\zeta^2\right)\eta^2 - 16\left(1 - \zeta^2\right) = 0, \tag{2.34}$$

where $\eta = \frac{c_R}{c_S}$ and $\zeta = \frac{c_S}{c_L}$. This equation has six roots which only depend on the Poisson's ratio ν for an elastic medium. However, according to Viktorov [23] the only root that has sense in a physical way - which implies $0 < \eta < 1$ and $0 < \nu < 0.5$ - can be approximated by

$$\eta_R = \frac{0.87 + 1.12\nu}{1 + \nu}. \tag{2.35}$$

This leads to a Rayleigh wave velocity of

$$c_R = \frac{0.87 + 1.12\nu}{1 + \nu} c_S. \tag{2.36}$$

Using a common Poisson's ratio of $\nu = 0.3$, equation (2.36) yields a Rayleigh wave velocity of $c_R = 0.93 c_S$. Moreover, it can be shown, that for any Poisson's ratio $0 < \nu < 1$ the Rayleigh wave velocity is smaller than the shear wave velocity and hence, also than the longitudinal wave velocity.

Equation (2.33) also shows that the Rayleigh wave velocity does not depend on the frequency of the propagating wave. This yields that Rayleigh waves are nondispersive.

As mentioned earlier, SAWs and therefore also Rayleigh waves have the property to decay exponentially with depth. According to Aschenbach [2], the stresses and displacements of Rayleigh waves are negligible at a depth of approximately $z = 1.5\lambda$. For a typical Rayleigh wave velocity in steel of $c_R \approx 2950\ \frac{m}{s}$ and typical excitation frequencies in nondestructive testing 1 MHz$< f <$10 MHz we look at wavelengths of $0.3\ mm < \lambda < 3\ mm$ depending on the excitation frequency. This energy concentration near the surface makes Rayleigh waves perfectly suitable to examine surface defects and therefore a powerful tool in ultrasonic nondestructive evaluation.

2.4 Excitation of Rayleigh Surface Waves

The excitation of Rayleigh surface waves in this research is performed using a Rayleigh wedge. This so-called prismatic coupling block method is widely used as conventional

ultrasonice transducers emitting longitudinal waves are used for wave generation. The concept is to generate longitudinal waves in a prismatic body usually made of quartz or plexiglass. As these longitudinal waves impinge the wedge-sample interface in a certain angle, Rayleigh waves are generated in the sample. The required angle for Rayleigh wave generation can be calculated using Snell's law

$$c_1 \sin\theta_2 = c_2 \sin\theta_1. \tag{2.37}$$

As depicted in figure (2.4) c_1 and θ_1 are the wave speed and angle of the incident whereas c_2 and θ_2 the wave speed and angle of the transmitted wave.

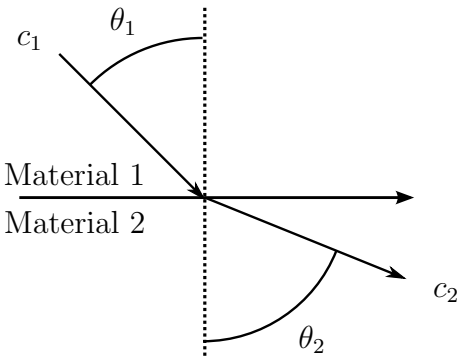

Figure 2.4: Snell's law for transmission

For the calculation of the Rayleigh angle, we assume c_1 and c_2 to be the the longitudinal wave speed in the wedge c_L^{wedge} and the Rayleigh wave speed in the sample c_R^{sample}. Since Rayleigh waves propagate on the surface we further assume $\theta_2 = 90$ and denominate $\theta_1 = \theta_R$ as the Rayleigh angle of the wedge. This yields

$$\theta_1 = \theta_R = \arcsin \frac{c_L^{wedge}}{c_R^{sample}}. \tag{2.38}$$

One can easily see, that this equation only holds for $c_L^{wedge} < c_R^{sample}$ which indicates that the wedge hast to be fabricated of material with a much slower wave speed than the sample. As already mentioned earlier, for steel samples quartz and plexiglass is suitable as wedge material.

2.5 Nonlinear Wave Propagation

This section discusses the nonlinear elastic wave theory, in particular the differences to the earlier discussed linear elastic wave propagation theories in this chapter. Linear wave propagation is an idealistic process. In reality, there are a variety of effects that cause a nonlinear behaviour in propagating waves, e.g. material defects or induced friction. A characterizing property that can be observed in nonlinear wave propagation is the conversion of energy to higher harmonic waves. In the following, this characteristic is introduced by means of a one-dimensional nonlinear P-wave propagating through a solid on the basis of Hamilton and Blackstock [12] as well as Viswanath [24].

For the means of explaining nonlinear wave propagation theory it is more convenient to express the stress-strain relationship in Lagrangian (or material) instead of Eulerian (or spatial) coordinates. The displacement $\mathbf{u} = \mathbf{x}^* - \mathbf{x}$ is the deviation of a particle's current position $\mathbf{x}^*$ from its original position $\mathbf{x}$ in undeformed state. The spatial and the material description can be related using the deformation gradient tensor

$$\mathbf{F} = \frac{\partial \mathbf{x}^*}{\partial \mathbf{x}} = \mathbf{I} + \frac{\partial \mathbf{u}}{\partial \mathbf{x}}, \tag{2.39}$$

where $\mathbf{I}$ is the identity tensor. Using the deformation gradient tensor, we can define the Lagrangian strain tensor

$$\mathbf{E} = \frac{1}{2}\left(\mathbf{F}^T \cdot \mathbf{F} - \mathbf{I}\right). \tag{2.40}$$

Rewritten in index notation the Lagrangian strain can be expressed as

$$\mathbf{E} = \frac{1}{2}\left(\frac{\partial u_i}{\partial x_j} + \frac{\partial u_j}{\partial x_i} + \frac{\partial u_k}{\partial x_i}\frac{\partial u_k}{\partial x_j}\right). \tag{2.41}$$

Furthermore, we can introduce the first Piola-Kirchhoff stress tensor

$$\mathbf{P} = \frac{\rho_0}{\rho}\boldsymbol{\sigma} \cdot \mathbf{F}^{-\mathbf{T}}, \tag{2.42}$$

where ρ_0 denotes the density of the undeformed and ρ the density of the deformed body. Using this definition of the first Piola-Kirchhoff stress we can rewrite the equation of motion (2.5) in Lagrangian (or material) coordinates while still neglecting body forces as

$$P_{ij,j} = \rho_0 \ddot{u}_i. \tag{2.43}$$

Furthermore, we introduce the specific strain energy per unit mass W of the elastic body defined as

$$\mathbf{P} = \rho_0 \frac{\partial W}{\partial \mathbf{F}}. \tag{2.44}$$

Assuming that the strain energy density depends on the local stretching and volume change, which holds for most materials, W is a function of the Lagrangian strain tensor only ($W = W(\mathbf{E})$). In this case, the relationship between the first Piola-Kirchhoff stress and the strain energy density can be rewritten as

$$\mathbf{P} = \rho_0 \mathbf{F} \cdot \frac{\partial W}{\partial \mathbf{E}}. \tag{2.45}$$

According to Hamilton and Blackstock [12] we can assume the following expansion for W in case of small, but not infinitesimal strains:

$$\rho_0 W = \frac{1}{2!} C_{ijkl} E_{ij} E_{kl} + \frac{1}{3!} C_{ijklmn} E_{ij} E_{kl} E_{mn} + O, \tag{2.46}$$

where O denotes higher order terms that can be neglected under the assumption of small strains. C_{ijkl} and C_{ijklmn} are the second and third order moduli. Using this equation and the symmetry of the Lagrangian strain tensor, we can express the Piola-Kirchhoff stress as

$$P_{ij} = C_{ijkl} \frac{\partial u_k}{\partial x_l} + \frac{1}{2} M_{ijklmn} \frac{\partial u_k}{\partial x_l} \frac{\partial u_m}{\partial x_n}, \tag{2.47}$$

with

$$M_{ijklmn} = C_{ijklmn} + C_{ijln}\delta_{km} + C_{jnkl}\delta_{im} + C_{jlmn}\delta_{ik}. \tag{2.48}$$

Substituting this in the Lagrangian equation of motion (2.43)we obtain

$$\rho_0 \frac{\partial^2 u_i}{\partial t^2} = \frac{\partial^2 u_k}{\partial x_j \partial x_l} \left(C_{ijkl} + M_{ijklmn} \frac{\partial u_m}{\partial x_n} \right). \tag{2.49}$$

Reducing this problem to a one-dimensional P-wave propagating, we can simplify equation (2.49) to

$$\frac{\partial^2 u}{\partial t^2} = A \frac{\partial^2 u}{\partial x^2} + B \frac{\partial^3 u}{\partial x^3}, \tag{2.50}$$

where A is the coefficient of the second order term, depending on the second order elastic modulus C_{ijkl} and B is the coefficient of the third order term resulting from a combination of the second order modulus (C_{ijkl}) and the introduced tensor (M_{ijklmn}). According to Kim et al. [14], a solution to the partial differential equation (2.50) is given by

$$u(x,t) = A_1 \sin(kx - t) - \frac{1}{8} \frac{B}{A} k^2 A_1^2 x \cos[2(kx - t)] + O. \tag{2.51}$$

The second term of the solution, obviously, is an expression for a second harmonic wave. O is the sum of all higher harmonic waves propagating in the material which are neglected for the further investigation.

2.5.1 The Nonlinearity Parameter β

Considering equation (2.51) we can establish an expression for the second harmonic amplitude

$$A_2 = \frac{1}{8} \frac{B}{A} k^2 A_1^2 x. \tag{2.52}$$

Furthermore, we define a nonlinearity parameter $\beta = \frac{B}{A}$ and rewrite (2.52) solving for β:

$$\beta = \frac{8}{k^2 x} \frac{A_2}{A_1^2}. \tag{2.53}$$

Thus, it is obvious that the nonlinearity parameter β describing the nonlinear stress-strain relationship of a material can be experimentally determined by measuring the

amplitudes of the fundamental and second harmonic waves propagating in the material. As this result was derivated using a one-dimensional propagating wave, it is only valid for one-dimensional longitudinal waves. However, according to Green [11] and Norris [19], the acoustic nonlinearity for shear waves in an isotropic material regarding the third order elastic constants is negligible due to symmetry of the second and third order moduli. Since Rayleigh waves involve a combination of longitudinal and shear displacement, it can be concluded that the longitudinal wave component is the sole source of the acoustic nonlinearity in Rayleigh waves. Therefore, we only regard material nonlinearity for longitudinal waves. As we keep the frequency constant for our measurements, we can further introduce a relative nonlinearity parameter

$$\beta' = \frac{A_2}{xA_1^2} \propto \beta. \tag{2.54}$$

Equation (2.54) reveals two different approaches to determine the nonlinearity parameter:

1. we can vary the excitation amplitude A_1 and measure at a specific propagation distance x away from the source

2. or we can vary the propagation distance x while keeping the excitation amplitude A_1 at a constant value.

Both approaches involve advantages and disadvantages for the experimental setup and the measurement procedure.

2.5.2 Nonlinear Rayleigh Wave Propagation

The principle of nonlinear wave propagation was described for a one-dimensional P-wave propagating. However, similar equations can be derived for the propagation of a Rayleigh surface wave on the basis of Herrmann et al. [13]. Recalling the displacement potentials ϕ and ψ and the relationship of their amplitudes B_1 and C derived applying

stress free boundary conditions

$$\varphi = -i\frac{B_1}{k_R}e^{-pz}e^{i(k_Rx-\omega t)} \tag{2.55}$$

$$\psi = -i\frac{C}{k_R}e^{-sz}e^{i(k_Rx-\omega t)} \tag{2.56}$$

$$B_1 = -i\frac{2k_Rp}{k_R^2+s^2}C, \tag{2.57}$$

we can decompose the displacement of the propagating wave into its longitudinal (in x-direction) and shear (in z-direction) components:

$$u_x = B_1\left(e^{-pz} - \frac{2ps}{k_R^2+s^2}e^{-sz}\right)e^{i(k_Rx-\omega t)} \tag{2.58}$$

$$u_z = iB_1\frac{p}{k_R}\left(e^{-pz} - \frac{2k_R^2}{k_R^2+s^2}e^{-sz}\right)e^{i(k_Rx-\omega t)}. \tag{2.59}$$

According to Herrmann et al. [13], the second order harmonic Rayleigh wave in a medium with weak quadratic nonlinearity and sufficiently large propagation distance can, then, be approximated by the displacements

$$u_x \approx B_2\left(e^{-2pz} - \frac{2ps}{k_R^2+s^2}e^{-2sz}\right)e^{2i(k_Rx-\omega t)} \tag{2.60}$$

$$u_z \approx iB_2\frac{p}{k_R}\left(e^{-2pz} - \frac{2k_R^2}{k_R^2+s^2}e^{-2sz}\right)e^{2i(k_Rx-\omega t)}. \tag{2.61}$$

For the conducted measurements, the out-of-plane displacement, so the displacement in z-direction u_z, at the sample surface is measured. A relationship between the fundamental and second harmonic amplitude of the displacement in z-direction can be derived using equations (2.59) and (2.61) and the definition of the nonlinearity parameter β established for P-waves:

$$\frac{u_z(2\omega)}{u_z^2(\omega)} = \frac{\beta k_l^2 x}{8i\frac{p}{k_R}\left(1-\frac{2k_R^2}{k_R^2+s^2}\right)}, \tag{2.62}$$

where $u_z(\omega)$ and $u_z(2\omega)$ denote the displacements of the first and second harmonic. Solving this equation for the nonlinearity parameter β yields

$$\beta = \frac{8ip}{k_l^2k_R}\left(1-\frac{2k_R^2}{k_R^2+s^2}\right)\frac{u_z(2\omega)}{xu_z^2(\omega)}. \tag{2.63}$$

Similar to the case of a P-wave propagating, for a constant frequency ω the first part of this equation becomes a constant and we can establish a relative nonlinearity parameter β':

$$\beta' = \frac{u_z(2\omega)}{x u_z^2(\omega)} \propto \beta. \tag{2.64}$$

For the sake of convenience, the out-of-plane displacement amplitudes of the first and second harmonic will be denoted as $A_1 = u_z(\omega)$ and $A_2 = u_z(2\omega)$ in the following. Thus, we can rewrite equation (2.64) as

$$\beta' = \frac{A_2}{x A_1^2} \propto \beta. \tag{2.65}$$

CHAPTER III

SENSITIZATION AND STRESS CORROSION CRACKING

The goal of this research is to investigate stress corrosion cracking (SCC) using Rayleigh surface acoustic waves presented in section (2.3). The following chapter briefly covers the issue of SCC damage and gives an overview of its cause, impact and the changes that happen in the material due to stress corrosion. In the end, the conditioning of the samples used for this research are presented with an expected impact on the Rayleigh measurements.

3.1 Source and Impact of Stress Corrosion Cracking

Stress corrosion cracking is a complex mechanism involving chemical reactions of a metallic base material with an aggressive surrounding medium in a region of localized plastic strain. Although this sounds like a very particular process, it can occur under a variety of conditions. The surrounding medium causing stress corrosion, is not restricted to highly aggressive solutions, but SCC can also be caused by a very mildly corrosive atmosphere, e.g. by the very low amount of chlorides in tap water [21], or by salt present in humid air in coastal regions and accordingly offshore areas [6]. Furthermore, SCC does not only occur in corrosion susceptible materials, but under certain conditions also in corrosion resistant materials such as 304 stainless steel (304 SS) which is used in this research. The plastic strain which is required for SCC must not be applied extensively, but it is sufficient if it is present in a highly localized area. Therefore, SCC is deemed an "insidious" process that can arise unexpectedly

by Staehle [21].

Stress corrosion can initiate microcracks in regions of localized plastic strain, while on a macroscopic scale the applied stresses are lower than the yield stress. These microcracks can grow larger and initiate macroscopic cracking of the material which reduces the structural integrity of a component. These processes and especially the speed of the SCC process depends on a variety of parameters. Some of these parameters, like the ambient medium, the applied stress and the operating temperature might be well known and controllable. However, there are also some that are difficult to quantify, e.g. residual stresses in the material due to fabrication that lead to localized plastic strains, inhomogeneities in the microstructure of the base material or varying environmental parameters like air humidity or temperature. Therefore, SCC is considered a relatively "unpredictable process" [6].

To ensure safe operation of a device under operating conditions that facilitate SCC, it is important to detect SCC damage in its early stages, before it affects the structural integrity of the device.

3.2 The process of Stress Corrosion Cracking

Taking a closer look at the process of SCC, first of all, one can distinguish between two different kinds of SCC:

Transgranular SCC (TGSCC) directly attacks the metallurgic structure in the grains. This means, the crack path runs through the grains. In an austenitic stainless steel, which is used as base material for this research, TGSCC "is usually associated with chloride-contaminated aqueous environments" [8]. The cracks initiated are characterized by a multi-branched path that looks like lightning bolts. Figure (3.1) shows an exemplaric microscopic picture of a transgranular crack.

Intergranular SCC (IGSCC) attacks the grain boundaries of the metallurgic structure. The crack paths of intergranular SCC run along the grain boundaries and are

usually characterized by a single crack path. However, for intergranular cracks there are often more than one single isolated crack, since SCC still occurs on many locations in an area at the same time, so there exist various single branched cracks. In austenitic stainless steels, IGSCC typically occurs in presence of a "sensitized" microstructure. The process of sensitization is a main issue for this work and is, therefore, explained in detail in a later section. Figure (3.1) shows a microscopic picture of a intergranular crack.

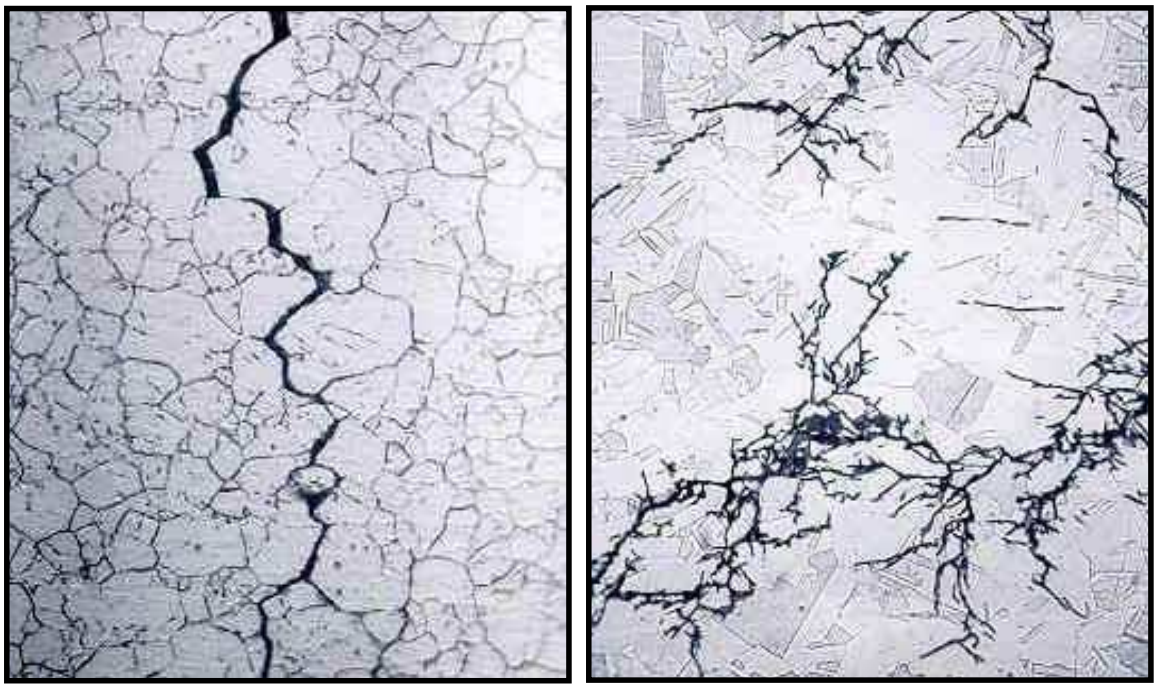

Figure 3.1: Microscopic picture of intergranular (left) and transgranular (right) SCC [17]

From an electrochemical point of view, one can further distinguish between anodic and cathodic SCC:

Anodic SCC is dominated by anodic metal dissolution. The chemical processes happening in the material is described in detail by Chen [7]. The metal atoms donate electrons which makes them positively charged ions that react with the surrounding

medium. Naturally, a passive oxide layer forms on the material surface that prevents further oxidation of the material. However, if mechanical stress is superpositioned with this chemical reaction, the passive layer flakes off at areas of high strain (localized plastic strain), i.e. at crack tips. In this case, a new active area is formed that reacts with the medium leading, for example, to the growth of already existing cracks. The anodic partial reaction takes place at these exposed areas, while the cathodic partial reaction mainly takes place at areas covered by the passive oxide layer. Anodic SCC typically occurs in stainless steels. Figure (3.2) shows a sketch of the chemical process of anodic SCC.

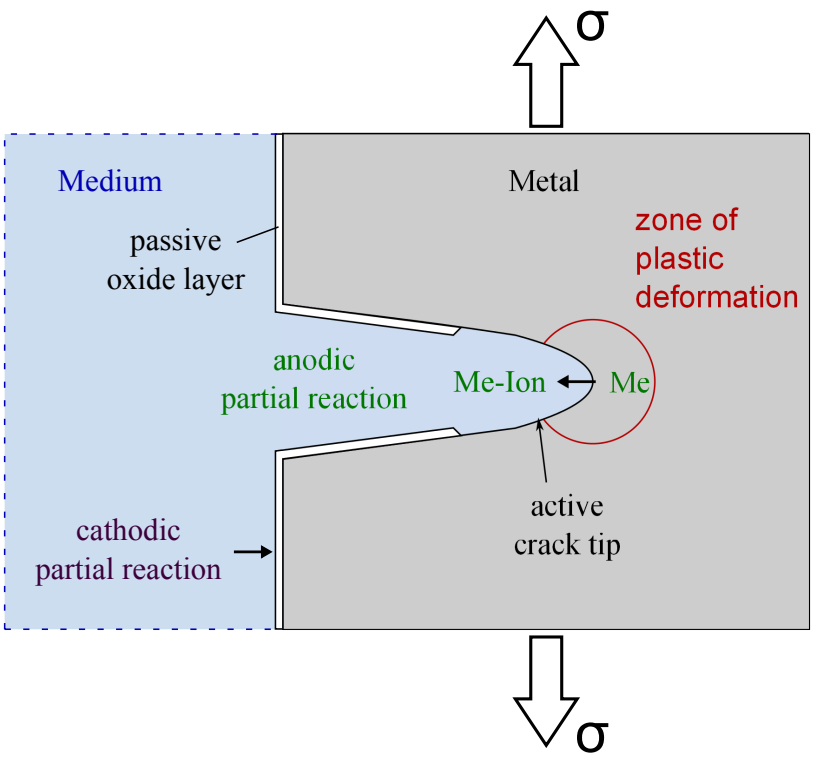

Figure 3.2: Anodic SCC

Cathodic SCC is dominated by molecular hydrogen (H_2) production in the surrounding medium. The anodic dissolution of the material only proceeds slowly. The crack growth is mainly caused by hydrogen diffusion into the material which reduces

ductility of the material. This process is called hydrogen embrittlement. For this case of SCC, cracks can also be generated in the material, not solely on the surface depending on how deep the hydrogen diffuses into the material. Cathodic SCC typically occurs in high strength steels.

In this work, sensitized 304 stainless steel is used, therefore, anodic intergranular SCC will be introduced in the material. The following section shall depict the process of sensitization which is a fundamental issue for intergranular SCC.

3.3 Sensitization

SCC can occur in corrosion resistant materials under certain conditions. The key factor respectively to SCC susceptibility is known to be the alloy composition. According to [6] one chemical constituent of a stainless steel that particularly affects SCC susceptibility is its carbon portion.

Considering austenitic stainless steel (e.g. 404 SS), the most common process known to increase SCC susceptibility is called sensitization. Sensitization occurs when the material is heated and held at temperatures between 400 and 800°C (752 and 1472°F). At these temperatures, carbon diffuses towards the grain boundaries where it reacts with present chromium to form chromium rich carbides. This process, called sensitization, reduces the pure chromium concentration at the grain boundaries; this chromium accounts for the material's corrosion resistance. Sensitization, therefore, is known to facilitate intergranular SCC occurring at the grain boundaries. As in all chemical processes, time is a key factor in sensitization. Hence, not only the temperature at which the material is held, but also the holding time affects the reduction of chromium concentration at the grain boundaries. Another factor known to influence the chromium concentration is the surrounding medium while the material is heated. Here, one can distinguish between heating under inert gas, heating with air

as the surrounding medium or heating under direct flame. In any case, once this pure chromium concentration at the grain boundaries drops under a certain value, the material becomes susceptible to intergranular SCC.

3.4 Welding as a cause of SCC

High temperatures that result in sensitization can to some extend be avoided during the operating state of a device. If extreme heating cannot be avoided, at least sensitization can be taken into account when a device is designed. However, there are also conditions where sensitization and later, during lifespan, SCC occurs in a more random fashion.

According to [6], sensitization can be induced in the so called heat affected zone (HAZ) during a standardized welding process. While welding, a material is heated excessively. During the cool-down phase there exists a time period where the material temperature is in the critical range of 400 to 800°C. Depending on the time span that the material temperature is in the critical range, the pure carbon concentration at the grain boundaries is reduced and the material becomes susceptible to intergranular SCC. Furthermore, welding processes in pipework can lead to residual stresses near the yield strength of the material, as it is shown by Assis [3]. These high residual stresses, superposed with mechanical stress during the operating state can lead to localized plastic strain. Consequently, welded areas fulfill all material-based requirements for stress corrosion. Therefore, research on SCC in welded components focuses on the damage in this close-to-weld regions, i.e. the HAZ. In this research, this is done by sensitization of the base material.

3.5 SCC in this research and its expected impact on material nonlinearity

Consider SCC and its expected impact on the relative nonlinearity parameter β' are presented.

The samples used in this research are cut out of a cold rolled 304 SS plate using water jet to prevent excessive heating. Note that cold work introduces a significant amount of dislocations in the material. Therefore, a high amount of dislocation density is expected in the fabricated samples. According to Matlack et al. [16], increasing dislocation density is known to increase the material nonlinearity.

In a first step, the samples are sensitized for one hour at a temperature of $650°C$ with air as surrounding medium. The impact of sensitization on the relative nonlinearity parameter is described in detail in [1], where sensitizing was performed at a similar temperature ($675°C$) with air as surrounding medium and for variable time of sensitizing. According to this paper, an increase in β' is expected to be observable due to the formation of chromium-carbide precipitates at the grain boundaries. However, sensitizing the material at this temperature also has a secondary effect. The sensitization temperature is similar to the stress-relief annealing temperature of 304 SS. Residual stresses of unknown magnitude are expected in the basic material due to the rolling of the plate and the blanking of the samples and one has to anticipate that stress-relief annealing will happen as a secondary effect of sensitizing. In [15] the effect of residual stresses in the material on the relative nonlinearity parameter β' are depicted. This research shows that residual stresses increase and therefore stress-relief annealing will decrease the relative nonlinearity parameter β'.

In addition to that, dislocation movement and annihilation is expected. As cold rolled stainless steel is the base material for this research a high dislocation density is expected. Dislocations are known to increase the material nonlinearity significantly [16]. Therefore, their annihilation will result in a decrease in β'.

Summarizing this, counteractive effects are occurring in this first process step. Due to the unknown magnitude of residual stresses and initial dislocation density, it is hard to predict if sensitization will result in an increase or a decrease of β'.

In a second process step, the SCC damage is introduced in the samples in a SCC cell. As already mentioned, in this research anodic intergranular SCC is expected to occur in the material since 304 SS is used with a Sodium Thiosulfate solution as aggressive medium. The microstructural changes and their influence on the relative nonlinearity parameter β' are rather complex for this process step. Firstly, due to the applied mechanical stress of yield strength and higher, dislocation motion and annihilation can further occur, depending on the remaining dislocation density after sensitization. This has been shown to result in a decrease of β' by Cantrell [5]. Similarly, loading the sample can further relieve remaining residual stresses in the samples. As the sample is exposed to the corrosive medium for a longer time, the medium will attack the grain boundaries and microcracks start to evolve in the material. These microcracks cause the so called clapping nonlinearity which increases acoustic nonlinearity. In the final stage of SCC damage, the microcracks spread, join each other and grow larger to form macroscopic cracks. Macroscopic cracks are characterized by large attenuation, especially concerning the second harmonic amplitude as it is much smaller than the first harmonic. Thus, in this last stage of SCC damage, a drop in the relative nonlinearity parameter would occur. However, in this research, the samples are corroded to a much lower level of SCC damage as we wish to detect early stages of SCC damage. This final stage where macrocracks are formed could also be observed using linear ultrasonic methods and is, therefore, not in the scope of this work.

CHAPTER IV

SPECIMENS AND PRELIMINARY MECHANICAL TESTS

4.1 Basic Thoughts

The scope of this research is to investigate the feasibility to characterize SCC damage in sensitized 304 SS devices using Rayleigh surface waves with the perspective to conduct similar research on actual welded components in the future as sensitization evokes similar microstructural changes in the material as welding does in the heat affected zone (HAZ). Regarding weldment, SCC damage is, therefore, known to mainly occur in the HAZ of the weld and not the weld material itself. Hence, a change in the material nonlinearity is expected to be observable. From a theoretical point of view, it would be attractive to investigate the nonlinear behavior of a wave propagating parallel to the weld in the HAZ as shown in figure (4.1).

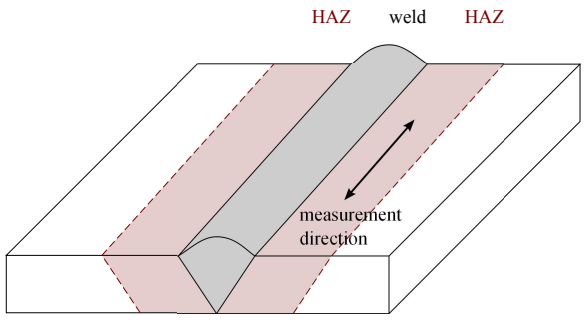

Figure 4.1: Idealized measurement method of SCC in welded devices using nonlinear wave propagation

The HAZ typically has a width of the same magnitude as the thickness of the welded material. Therefore, in order to obtain a sufficiently wide HAZ to perform

Rayleigh surface wave measurements, the material thickness has to be chosen accordingly large. However, to induce stress corrosion in a sample, the material has to be loaded at approximately yield strength. Thus, the mechanical load that needs to be applied to a sample, will be proportional to its cross section. This, of course, restricts the maximum material thickness that can be chosen.

Considering this restriction, the idea of preforming "cross-weld" measurements comes to the fore, where the wave is generated on the one and measurements are performed on the other side of the weld. For this type of measurement, the HAZ must not be wide enough, to have the wave propagating solely in it anymore. The idea is to generate a Rayleigh surface wave in the base material on one side of the weld, have it propagate through the near HAZ, the weld itself and the far HAZ and perform measurements on the base material on the other side of the weld. Figure (4.2) shows a schematic of the cross-weld measurement. As depicted in the graphic, this experiment could be performed on a thin plate of relatively small cross section.

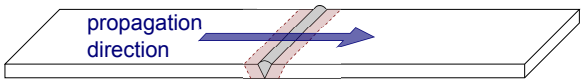

Figure 4.2: schematic of the idea of a cross-weld measurement

For purposes of a homogeneous weld and reducing weld differences in multiple samples, the weld can be manufactured in a big plate before the samples are cut out as depicted in figure (4.3).

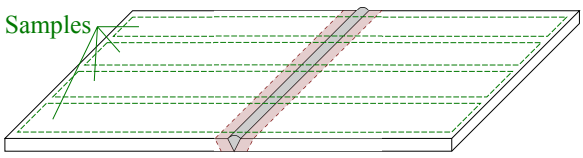

Figure 4.3: fabrication of multiple samples with homogeneous welds

However, the cross-weld measurements also have a downside: The propagating

wave has to pass through the welded area. Due to the different microstructure of the weld material, the wavefield is expected to become scattered and reflected when passing through it. The magnitude of the scattering and the feasibility to conclude from cross-weld measurements to the level of SCC damage in the HAZ has yet to be determined.

As stated above, the greater aim of this research section is to investigate the possibility to quantify the amount of SCC damage in the HAZ of welded components. Due to the many uncertainties concerning the scattering of the wave field in the weld, especially regarding cross-weld measurements, this work focuses on the processes happening in the HAZ and therefore "simulates" the HAZ of a weld by solely sensitizing the base material to a certain degree instead of using an actual weld. Thus, the samples produced for the examination of SCC in this research are non-welded sensitized samples. However, as an outlook, in addition to the sensitized samples, also some welded samples are fabricated using the proposed method displayed in figure (4.3).

4.2 Specimens

This section depicts the fabrication and preconditioning of the used samples, since this is an important factor for SCC as it is already stated in the previous chapter. The base material for all samples is cold rolled 304 stainless steel. 304 SS is a typical material used in pipework of power plants. Table (4.1) shows the composition and table (4.2) the main mechanical properties of the alloy used in this work.

Table 4.1: Composition of 304 SS

Element	C	Mn	P	S	Si	Cr	Ni
Percentage (%)	0.08	2.0	0.045	0.03	0.75	18-20	8-12

Table 4.2: Mechanical properties of 304 SS

Yield strength (MPa)	290
Tensile strength (MPa)	621

4.2.1 Geometry

Mostly, constraints due to the experimental procedure determined the geometry of the specimens used in this research. Since the SCC cell applies a tensile force, a dogbone-like shape provided the most simple and effective geometrical solution. The intention to perform Rayleigh measurements on the sample surface imposed a restriction on the minimal width of the samples. The thickness of the plate from which the specimens were cut out, was then defined by the maximal force, the loading cell of the SCC setup can apply which limited the maximal cross-section of the sample. The length of the samples needed to be chosen long enough to perform Rayleigh measurements on the deformed part of the sample. For these measurements, usually a length of 100 mm is sufficient. However, the samples were fabricated longer, to have the possibility to perform measurements on different positions on the sample. Figure (4.4) shows a draft of the produced samples.

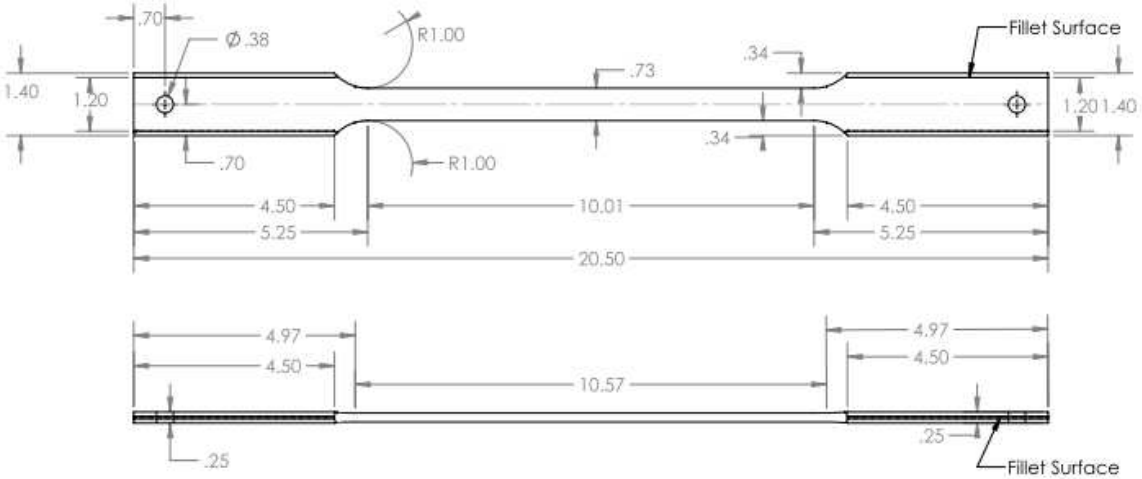

Figure 4.4: Draft of 304 SS samples

As already mentioned, the specimens are cut out of a 304 SS Plate using water jet to prevent an excessive increase in temperature. In a following step, the samples are ground and polished using sandpaper of different grid, increasing up to 800 grid. Part of the samples went through the process of sensitizing and stress corrosion. However, some were left untreated as reference samples. Furthermore, as mentioned earlier, some welded samples for outlook purposes were fabricated too.

4.3 Sensitization

As stated in chapter (3), preconditioning plays an important role for SCC to happen. The samples experienced heat treatment before they were polished to 800 grid and prepared for SCC. The heat treatment was performed in an oven with air as surrounding medium. Here, the samples were heated to $650°C$ $(1202°F)$ and held at this temperature for one hour. Preliminary tests on small tensile samples showed that this preconditioning paired with the chosen solution was sufficient to induce SCC in the material.

4.4 Stress Corrosion Setup

This section depicts the process of introducing stress corrosion into the material. However, for SCC to happen, certain parameters must be fulfilled. In this chapter, firstly, some preliminary tests to identify important parameters for the SCC setup are described, before the actual setup of the stress corrosion cell is presented.

4.4.1 Choice of corrosive medium and slow strain rate testing

In a first step, the corrosive medium is chosen. Important for the choice of the corrosive medium is the ability to introduce SCC in 304 SS at room temperature.

This restriction is made because not all welded parts in a power plant's pipework are operated at an elevated temperature. Furthermore, a chloride free solution is desirable. Considering these restrictions, a 0.5 molar Sodium Thiosulfate solution is chosen to introduce SCC to the material. Newman et al. [18] have shown, that a Sodium Thiosulfate solution introduces intergranular anodic SCC damage in 304 SS. However, to determine the correlation between the medium and the required degree of sensitization, preliminary corrosion tests on several tensile rods are performed.

Slow Strain Rate Testing (SSRT)

SSRT is performed to identify an appropriate sensitization time for the earlier constituted 0.5 molar Sodium Thiosulfate solution. In order to approximate the processes during welding the goal is to keep the sensitzation time at a minimum value. For this test, 304 SS rods are held at a temperature of $650°C$ between 0 and 8 hours. Subsequently, they are air-cooled to room temperature. After this sensitization process, the samples are polished, cleaned and set up in a SSRT machine using Sodium Thiosulfate as surrounding medium. The machine deforms the samples at a strain rate of approximately $10^{-6}\frac{1}{s}$ until rupture. Thereafter, the fracture surface as well as the elongation is examined. Figures (4.5) and (4.6) show the setup of the SSRT machine.

Figure 4.5: SSRT machine

Figure 4.6: SSRT corrosion cell

Figures (4.7)-(4.10) show the broken SSRT tensile rods after testing them. As expected, the non-sensitized sample does not show any form of SCC. On the other hand, the long-term sensitized samples (1 and 8 hours of sensitizing) show clearly visible corrosion damage circled in red.

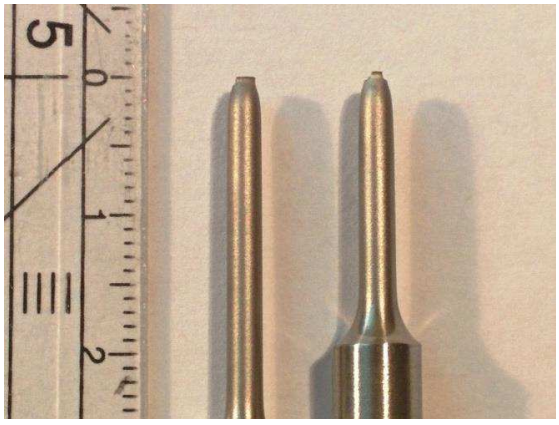

Figure 4.7: No sensitization

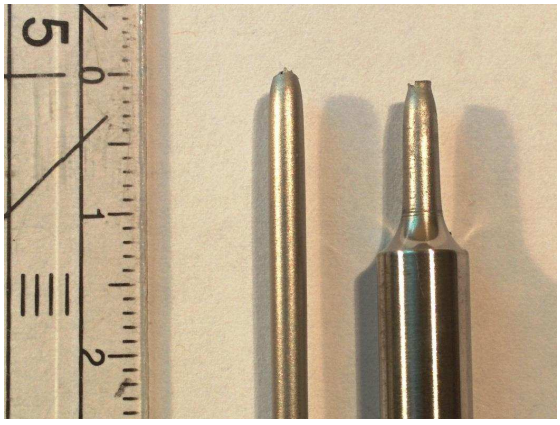

Figure 4.8: 10 minutes sensitization

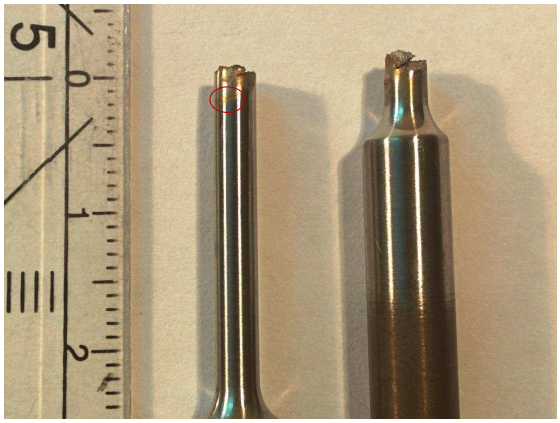

Figure 4.9: 1 hour sensitization

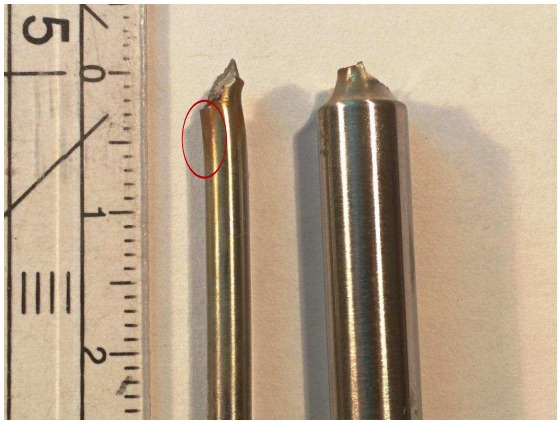

Figure 4.10: 8 hours sensitization

Furthermore, it can be seen that SCC causes embrittlement of the material and material failure at lower final strain rates. This becomes obvious when examining the final strains in figure (4.11). Here, the four samples with different durations of sensitization are organized with increasing rate of sensitization from left to right.

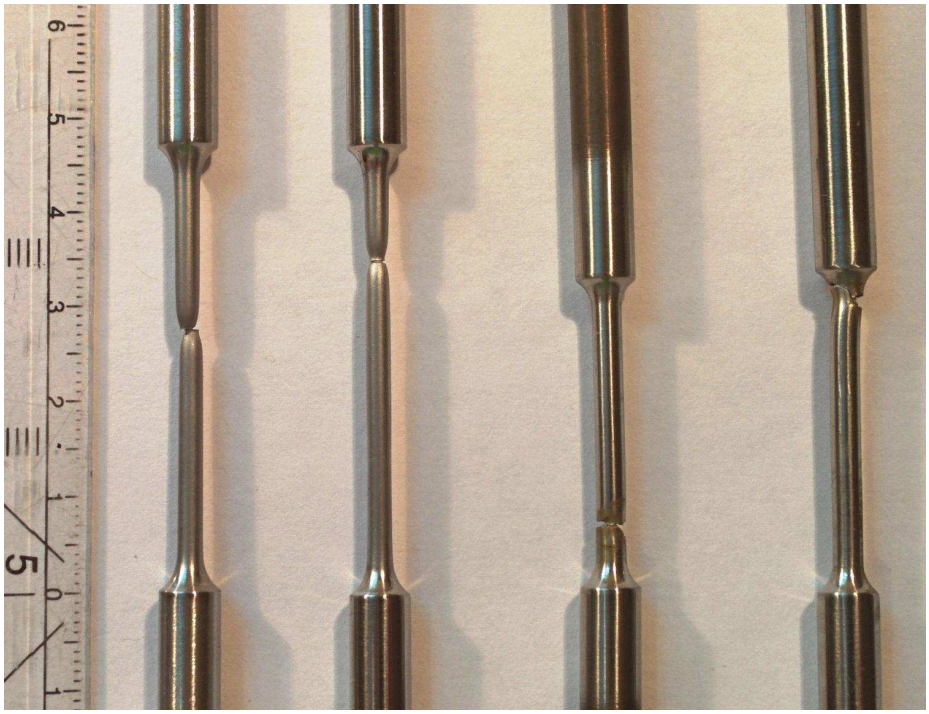

Figure 4.11: Samples after SSRT with increasing rate of sensitization from left to right

This preliminary experiment shows that it is possible to introduce SCC in 304 SS at room temperature using Sodium Thiosulfate as surrounding medium. However, the material has to be sensitized first to make it susceptible to SCC.

4.4.2 Determination of Applied Stress

Another important factor for SCC to happen, is the present stress in the material. As already stated earlier, SCC primarily happens in areas of localized plastic strain. In a welded device, this localized plastic strain could be given by a superposition of residual stress due to the welding process and a relatively low operational stress (lower than yield strength).

The non-welded material however, is expected to have a relatively low amount of

residual stress, since it has been fabricated using water jets to prevent excessive heating and it has been heat-treated afterwards during the sensitizing process. Therefore, a relatively high mechanical stress (approximately yield stress) has to be applied during the SCC experiment to cause localized plastic strain in the material. On the other hand, the goal is to induce damage due to stress corrosion and not due to excessive mechanical load.

In earlier researches, e.g. by Zeitvogel et al. [25], it has been shown, that values for the applied stress of $105\% - 110\%$ of yield strength are suitable to perform SCC tests. On the base of this research, the applied mechanical load is constituted to 105% and 110% yield strength - two different sets of corroded samples are produced. Reference values for the yield strength of 304 SS are $R_{p0.2} = 290\ MPa$ or $R_{p0.2} = 42\ ksi$ provided as minimum values by the supplier. However, due to fabrication issues, there are oftentimes deviations in yield strength, so a tensile test is conducted to determine the yield strength experimentally.

Figure (4.12) shows the load-extension curve obtained by a regular tensile test on one of the 304 SS samples and the calculated 0.2% yield strength.

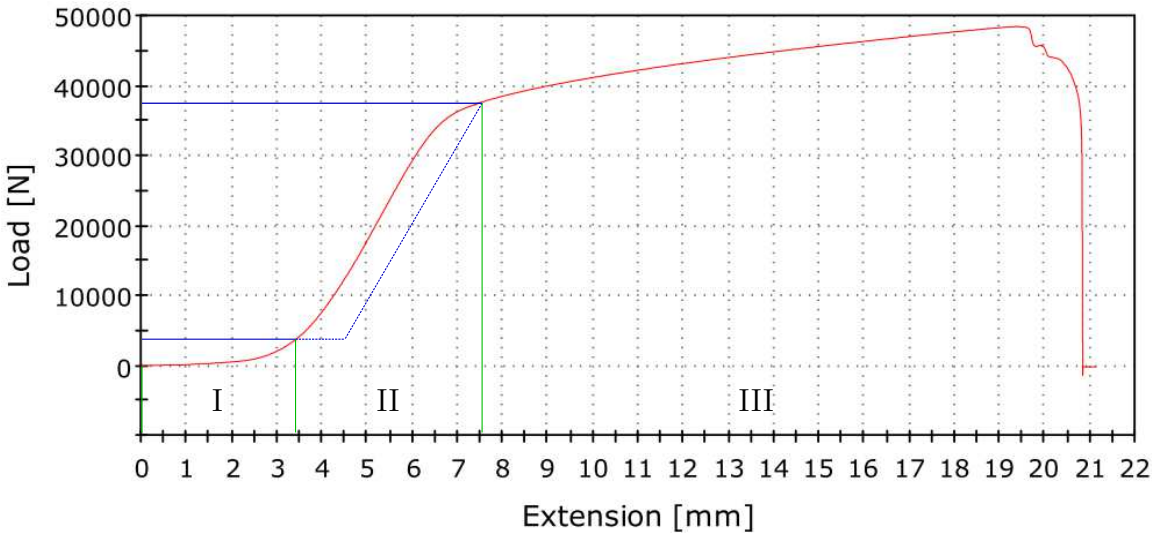

Figure 4.12: Load-Extension Curve

Here, in section I of the test, the grip between the holding mechanism and the sample is built up and slack is removed. In section II, the sample is deformed elastically and plastically up to a plastic deformation of 0.2%. This section is followed by the plastic deformation in III until failure of the sample. From section II, the yield strength can be estimated to be reached at a load of $F \approx 33600N$. This value is slightly higher than the reference values from the literature. Calculating the load at yield strength using the reference value for the yield strength and the originally measured cross section of the sample before deformation, we obtain $F_R = 32780N$. For the purposes of this research, the actual yield strength must not be calculated, since the machine used for the SCC setup is a force controlled tensile machine with a measure of pounds of load. The result of this preliminary tensile test is that yield strength for the samples used is estimated to be reached at $7380lbs$ of load. Regarding that the mechanical stress applied on the samples is constituted to 105% and 110% yield strength, the applied load for the later described SCC setup is determined to be $7750lbs$ and accordingly $8150lbs$.

4.4.3 Stress Corrosion Setup

In the following section, the setup for the SCC cell is presented. Table (4.3) gives an overview over the already defined parameters for the SCC setup.

Table 4.3: SCC setup parameters

Sample Material	304 stainless steel
Surrounding Medium	Sodium Thiosulfate ($Na_2S_2O_3$) solution
Concentration	0.5 molar solution
Applied Mechanical Load	$7,750lbs \mathrel{\widehat{\approx}} 35kN$ or $8,150lbs \mathrel{\widehat{\approx}} 37kN$

Figures (4.13) and (4.14) show a photograph and a sketch of the experimental SCC setup. The load is applied by attaching weights onto a lever arm and measured

directly in front of the SCC cell. The SCC cell itself is a both sidedly sealed glass cylinder filled with 0.5 molar Sodium Thiosulfate solution. The samples are held at 105% or 110% yield strength respectively for different timespans. After removing the samples from the stress corrosion cell, they are cleaned using acetone and polished with 800 grid sandpaper for a second time. For the purpose of this research, samples with different treatments are fabricated:

Two samples are left completely untreated. Two other samples are sensitized but not corroded to estimate the influence of sensitization on the material nonlinearity. Additional to that, for each load level (105% and 110% of YS) samples are corroded for one, three and five weeks of holding time.

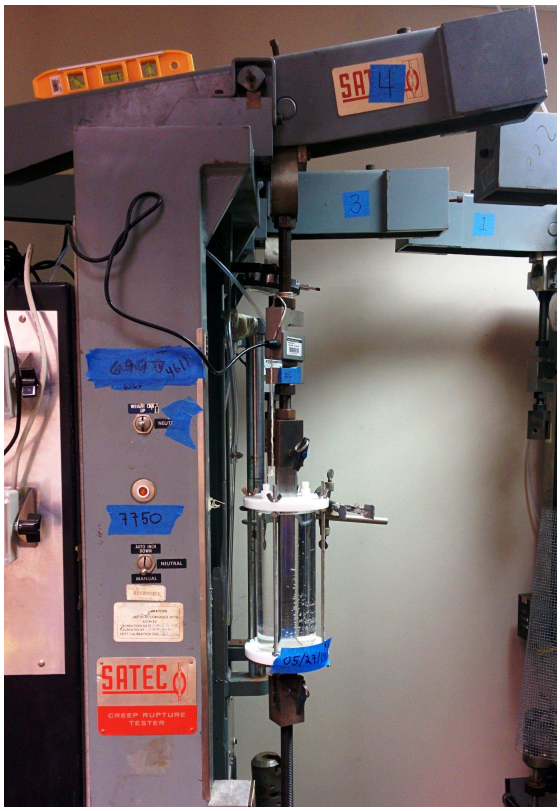

Figure 4.13: Photograph of SCC setup

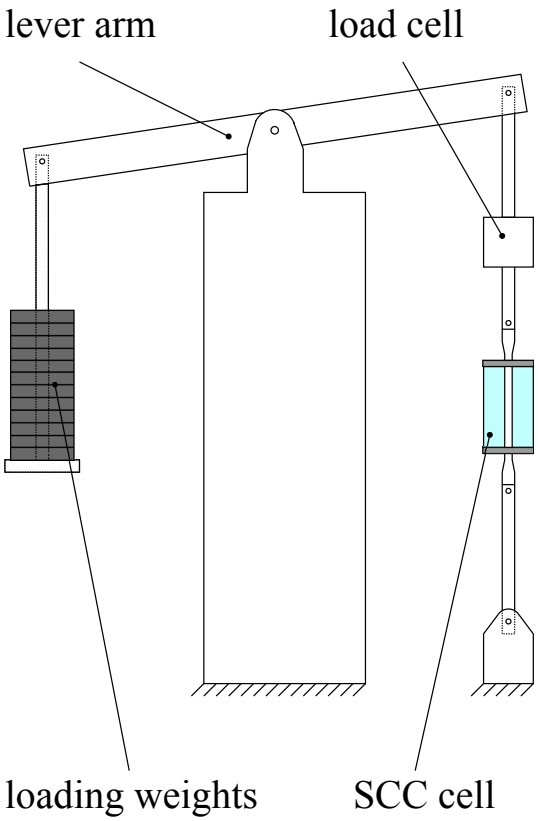

Figure 4.14: Sketch of SCC setup

CHAPTER V

NONLINEAR RAYLEIGH WAVE MEASUREMENTS

This chapter describes the nonlinear Rayleigh surface wave measurement procedure and the measurement setup. Two different methods are used to measure the nonlinear effects distorting a propagating Rayleigh wave in the SCC samples. The signal generation and excitation apparatus is the same for both measurement methods. However, the detection apparatus varies:

In a first set of measurements, air-coupled detection is used to measure "leaked" acoustic waves in the air. The leaked and measured signal is then post amplified and evaluated with an oscilloscope.

In a second set of measurements, wedge-detection is used to measure the amplitudes of the fundamental and second harmonic wave on the sample surface. The received signal is not amplified further and therefore can be evaluated with an oscilloscope directly.

Figure (5.1) shows a schematic of the measurement setup and its components. The used setup components and the measurement methodology are described in the following.

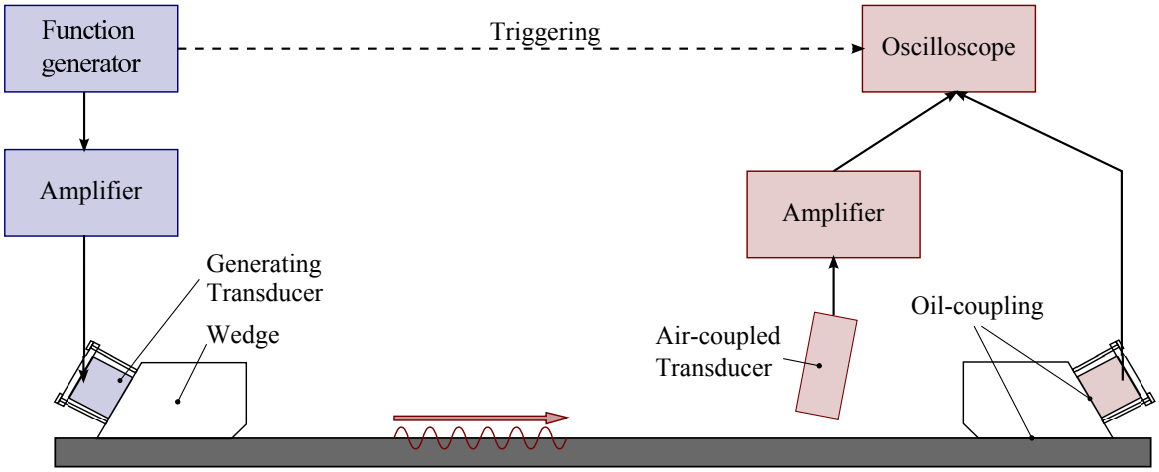

Figure 5.1: Schematic of the measurement setup

5.1 Setup Components

5.1.1 Function Generator

As depicted in figure (5.1), a function generator is used in this setup to provide a function for the excitation string, as well as to trigger the detection string. The function generator's output is a tone burst signal with a frequency of 2.1 MHz and a peak-to-peak voltage of 800 mV. Due to transient oscillation, the signal consists of 20 cycles in order to provide a sufficiently large steady state portion for the following signal processing. Furthermore, the function generator triggers the excitation string amplifier, called "RITEC", and the oscilloscope.

5.1.2 RITEC GA-2500A

The RITEC GA-2500A, a high power gated amplifier, is used to provide a high-voltage amplified signal for the affiliated transducer used in the excitation string. The high power signal enables the transducer to introduce waves with sufficiently high acoustic energy into the material in order to obtain a good signal-to-noise ratio for the later detected second harmonic component at the receiver. The RITEC GA-2500A provides a clean output signal with only little inherent nonlinearity. By granting this

device a warm up time of 30 minutes after it has been turned on, one can ensure a stable output signal during the measurement.

5.1.3 Transducers

In the excitation apparatus, a V-type piezoelectric half inch narrowband transducer with a nominal frequency of 2.25 MHz of the company Panametrics is used. The transducer converts the electrical signal obtained from the RITEC into longitudinal displacements. It, therefore, introduces a longitudinal or P-wave in the wedge.
The detection of these Rayleigh waves is accomplished with one of two different methods of detection, so different transducers are used. To obtain a high signal-to-noise ratio (SNR) for the second harmonic, the center frequency of the detecting transducer needs to match the second harmonic's frequency.
For the air-coupled detection, an Ultran NCT4-D13 air-coupled transducer with a nominal frequency of 4 MHz is used to detect leaked longitudinal waves in the air.
For the wedge detection, an A-type half inch broadband transducer with a nominal frequency of 5 MHz is used to detect longitudinal or P-waves in the wedge and convert it into an electrical output signal.

5.1.4 Rayleigh Wave Wedge

The purpose of the Rayleigh wave wedges is to convert a propagating P-wave in the wedge into the material in such a way, that a Rayleigh surface wave is generated in the specimen. The Rayleigh wave wedges for this research are made of Plexiglass and the geometrical design is constituted using Snell's law. The wedge angle θ_w is calculated using the known P-wave velocity in the wedge $c_P^{(wedge)}$ and the Rayleigh

wave velocity in the specimen $c_R^{(specimen)}$ as

$$\theta_w = \arcsin\left(\frac{c_P^{(wedge)}}{c_R^{(specimen)}}\right). \tag{5.1}$$

Figure (5.2) illustrates the wedge geometry with the attached transducer shown in blue. The black arrow indicates the P-waves emitted from the transducer and the red arrow indicates the by transmission generated Rayleigh waves.

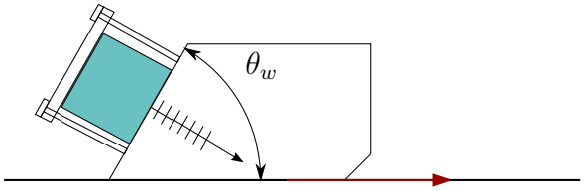

Figure 5.2: Geometry of the Rayleigh Wave Wedge

Light lubrication oil is used to acoustically couple the transducer and the wedge, as well as the wedge and the sample. A bar clamp provides the clamping force to attach the wedge to the sample. The clamping force influences the measurements significantly, so a constant clamping force is essential during the whole measurement and equivalent clamping forces are desirable when measuring various samples. Furthermore, settling effects are observed in the contact area resulting in a change of measured wave amplitude after joining the wedge to the sample. The settling effects are caused by changes in the oil film between the wedge-sample interface. Here, for example oil gets squeezed out of the contact area, thus reducing the layer's thickness and as well as changing the clamping force. In order to avoid these kind of discrepancies due to the settling effects, a waiting time of at least 10 minutes is used between attaching the wedge to the sample and first taking the ultrasonic measurements.

5.1.5 Detection Amplifier

For the air-coupled measurement method, the output of the air-coupled transducer is post amplified for further data processing. Here, a Panametrics 5676PR pulser-receiver is used for amplifying the signal by 40 dB.

5.1.6 Data Acquisition and Processing

The measured electrical signal is recorded by an oscilloscope and averaged over 256 different signals to improve SNR. Figure (5.3) shows a typical 256 time averaged signal.

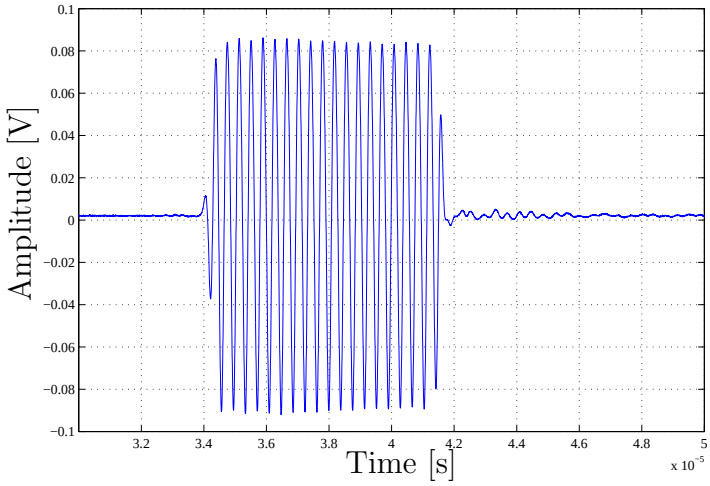

Figure 5.3: Averaged time signal over 256 sequences

The first step in calculating the fundamental and second harmonic amplitudes is to apply a Hann window in order to isolate the steady-state portion of the signal. Therefore, the first and last cycles of the propagating wave which typically include transients are neglected. Subsequently, the truncated data is transformed into frequency domain using a fast Fourier Transform (FFT) to obtain the amplitudes of the first and second harmonic. Figure (5.4) shows the windowed and transformed data.

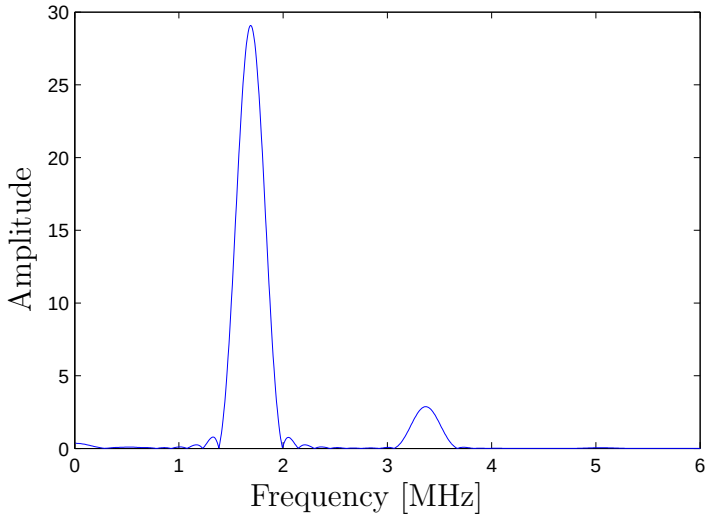

Figure 5.4: Hann windowed and Fourier transformed signal

Obviously, due to the windowing, the amplitudes of figure (5.4) do not match with the time signal (5.3) anymore. In order to calculate the real amplitudes, one has to use the formula

$$A_{real} = \frac{4 * A_{Hann}}{k} \tag{5.2}$$

where A_{real} and A_{Hann} are the actual and the Hann amplitudes and k is the number of datapoints included in the Hann window.

5.2 Measurement Procedure

5.2.1 Nonlinear System

The measurement system, instrumentation and coupling all contribute component-inherent nonlinearity to the measured ultrasonic waveform. Consequently, the function generator, the RITEC, the exciting transducer as well as the Rayleigh wave wedge and its interface with the sample all add system nonlinearity to the overall system's behavior. Similarly, the detection instrumentation including the second wedge with contact transducer or the air-coupled transducer with amplifier introduce nonlinear

effects into the detectd signal. Additionally, there is the material nonlinearity generated through nonlinear wave propagation as described in chapter (2) – isolation of this material nonlinearity from the system nonlinearity is the goal of effective nonlinear ultrasonic measurements. Figure (5.5) shows a schematic of the nonlinear system.

Figure 5.5: Schematic of the nonlinear system

The aim of these nonlinear ultrasonic measurements is to only measure the contribution from the material nonlinearity and use this to quantify the the degree of SCC damage. It is important to note that the material nonlinearity will increase with increasing propagation distance, while the instrumentation nonlinearity will remain constant with propagation distance. Therefore, we introduced the relative nonlinearity parameter β' relating the fundamental (A_1) and the second harmonic (A_2) amplitude of a propagating plane wave in chapter (2) as

$$\beta' = \frac{A_2}{xA_1^2}. \tag{5.3}$$

The goal of this research is to experimentally determine this relative nonlinearity parameter for samples with different levels of SCC damage. As stated earlier, amongst other microstructural changes the microcracks induced through SCC affect this nonlinearity parameter and a change is expected.

This research does not measure the absolute displacement amplitudes, but instead measures the amplitudes of the electric output current of the detecting transducer, equation (5.3) can be varied to

$$\beta' \propto \frac{A_2^{(el)}}{xA_1^{(el)_2}}. \tag{5.4}$$

Consequently, the relative nonlinearity parameter β' can be either determined by

varying the fundamental amplitude$A_1^{(el)}$, and thus, by varying the input voltage into the exciting transducer, or by varying the propagation distance x.

The inherent nonlinearity of the system can generate a second harmonic component with increasing input voltage. Instead, this research measures the change in the fundamental and second harmonic amplitudes as a function of increasing propagation distance. This way, the nonlinearity induced by excitation and detection components is kept approximately constant and the detected amplitudes give a more accurate measure of the material nonlinearity. A detailed comparison between these two measurement methods was done by Thiele et al. [22].

5.2.2 Air-coupled detection procedure

The relative nonlinearity parameter β' is estimated by measurements with varying propagation distance. The preliminary measurements of this research are performed on the basis of Thiele [22]. In Thiele's work, the alignment and angular calibration for air-coupled measurements are described in detail. Thiele emphasizes the importance of angular calibration and path calibration for this type of measurements. According to his work, the Rayleigh wave beam emitted from the generating transducer-wedge element has a Gaussian profile but due to fabrication and clamping discrepancy its peak must not necessarily propagate in a perpendicular line to the front edge of the wedge. Therefore in a preliminary calibration, the peak locations at the beginning and at the end of the measurement path are determined and during the later measurement, the air-coupled transducer is traversed linearly between these peak locations. Furthermore, the angular alignment of the air-coupled transducer is optimized for maximum perception in order to maximize the signal-to-noise ratio. This so-called Rayleigh angle α_R at which maximum perception occurs solely depends on the Rayleigh wave propagation speed and P-wave speed in air and is caused by interference of peaks

of different wave cycles. For steel, this angle typically lies around 6°. Figure (5.6) depicts the cause of this Rayleigh angle.

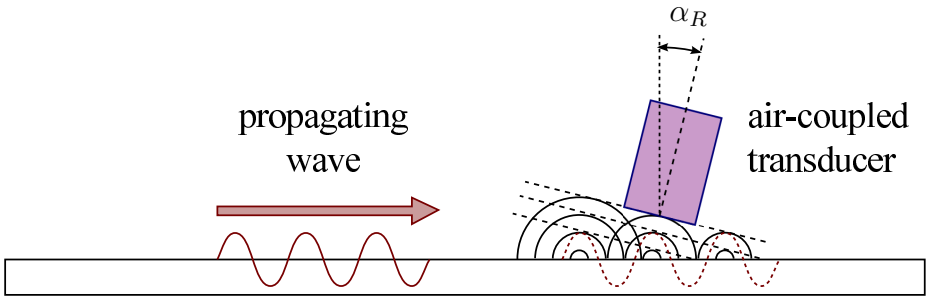

Figure 5.6: Rayleigh angle for maximum perception of the propagating wave

Once the setup is calibrated for maximum reception, the transducer is traversed linearly between the beginning and the end point. For the performed measurement, the frequency is held constant, therefore, we can neglect the proportionality of β' to the frequency. Furthermore, we can rewrite equation (5.4) to

$$\beta' = \frac{\Delta\left(\frac{A_2^{(el)}}{A_1^{(el)_2}}\right)}{\Delta\left(x\right)}. \tag{5.5}$$

This relationship reveals the principle of the measurement: The frequency, as well as the input in the generating transducer is held constant while the detecting transducer is traversed increasing the propagation distance of the Rayleigh wave. The detected first and second harmonic are, then, plotted over the propagation distance, as well as the ratio of $\frac{A_2^{(el)}}{A_1^{(el)_2}}$. The slope of this ratio over propagation distance x gives the relative nonlinearity parameter β'. Figures (5.7) and (5.8) show results for an aluminum reference sample.

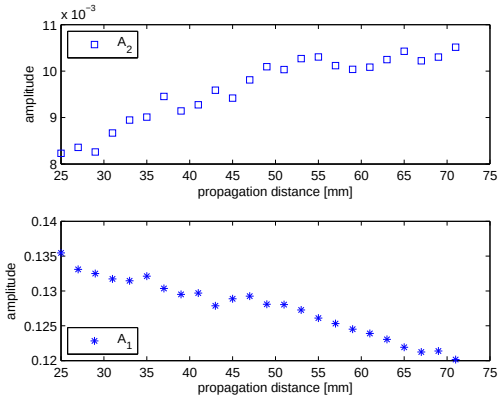

Figure 5.7: Amplitudes over propagation distance

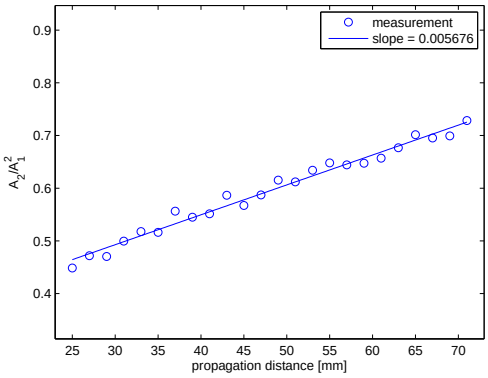

Figure 5.8: Ratio over propagation distance

5.2.3 Wedge detection procedure

Measurements with wedge detection are performed similarly to the previously described air-coupled detection: The wedge is traversed between a starting and an end point for the measurement. However, due to the transducer-wedge characteristics these measurements can be performed without calibration for the wave-peaks perpendicularly to the propagation distance. Rather than this, it is more important to align the detecting wedge front parallel to the generating wedge front at a certain distance. Obviously, there is also no need for any angle calibration, since the wedge angle is predetermined.

In this research, a fixture is attached to the wedge in order to align its center and the center axis of the transducers to the geometrical center of the samples. Note, that this does not necessarily imply, that the wedge is perfectly aligned to the acoustic axis. Figure (5.9) shows a sketch of the wedge alignment and the fixture.

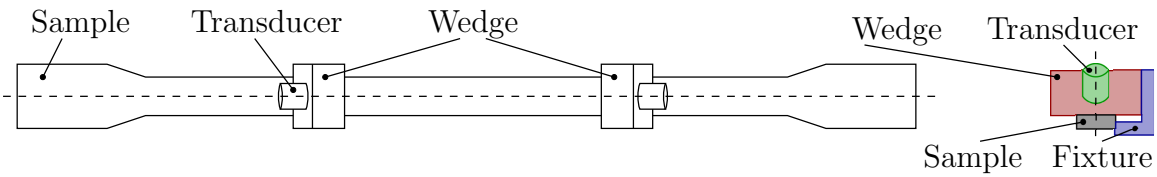

Figure 5.9: Allignment of Wedge and Sample center axes using a Fixture

No calibration prior to the measurement is needed for wedge-detection. However, the settling-time issues makes this measurement method extremely time-consuming. Satisfactory results are obtained only, if a waiting time of at least ten minutes after attaching the wedge to the sample is adhered.

Similar to the air-coupled method, the obtained first and second harmonic amplitudes and the ratio $\frac{A_2^{(el)}}{A_1^{(el)2}}$ are plotted over the propagation distance and the nonlinearity parameter β' is obtained evaluating the slope of the plotted ratio. Figures (5.10) and (5.11) show results obtained for one of the fabricated samples. Obviously, since the method is much more time-consuming than the air-coupled measurements, The number of evaluated points has to be decreased from 24 to 11.

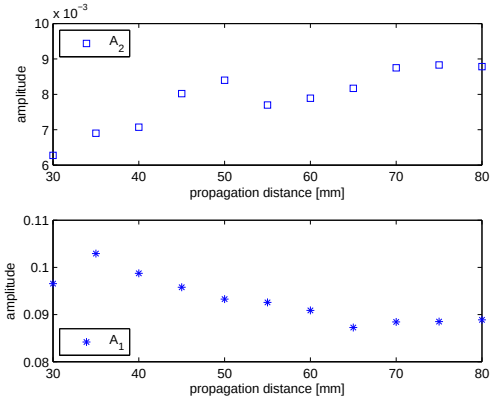

Figure 5.10: Amplitudes over propagation distance

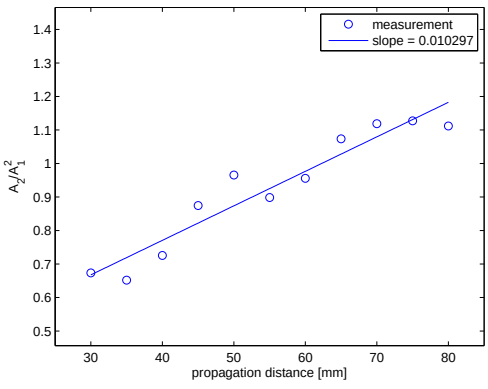

Figure 5.11: Ratio over propagation distance

CHAPTER VI

PRELIMINARY NONLINEAR ULTRASOUND RESULTS

This chapter presents the results of preliminary ultrasonic measurements; it compares air-coupled and wedge detection in terms of fundamental measurement advantages and disadvantages as well as their applicability to perform Rayleigh wave measurements on the proposed SCC samples. In addition, it presents the results from measurements on a welded 304 SS plate.

6.1 Comparison of Air-coupled and Wedge Detection

The measurement methodologies of air-coupled and wedge detection are explained in the previous chapter in detail. The goal of this section is to sum up the advantages and disadvantages of these two methods and show exemplary results for both.

As already mentioned, prior to the measurement, the air-coupled transducer needs to be adjusted for the optimal Rayleigh angle α_R and the acoustic axis needs to be found. In the case of wedge detection, the angular positioning is defined by the geometrical design of the wedge based on Snell's law. Furthermore, the axial alignment to the sample is given by the attached fixture. Hence, there is no calibration needed prior to wedge-detection measurements.

Measurements with non-contact detection can be performed very fast. Since the coupling conditions are not varying with time and there are no settling effects, the air-coupled transducer can detect displacements right after traversing. On the other hand, for the wedge detection, a settling time of at least 10 minutes after traversing and joining the wedge has to be adhered in order to obtain consistent results. This makes wedge detection measurements very time-consuming.

Another advantage of the air-coupled transducer is its applicability in performing a 2D-scan. In the case of a 2D-scan, the trend in the relative nonlinearity parameter is not only measured along the acoustic axis, but over a two dimensional area. This can provide advantages regarding the full characterization of the generated wave field.

Unfavorable for air-coupled detection is the low signal-to-noise ratio. As the air-coupled transducer measures leaked acoustic waves in the air, the signal strength is rather weak and has to be post amplified. For the case of wedge detection, no post amplifier is needed.

Important for the conducted measurements is the averaging characteristic of the two methods. In an ideal case, one would like to measure the displacement at one specific point. However, both methods average the displacement over a certain area. The air-coupled transducer has a receiving diameter of $17mm$ and averages arriving P-waves in the air over part of this diameter. Unfortunately the averaging characteristic of the air-coupled transducer is not known precisely. In the case of wedge detection, the wedge-transducer combination averages over the whole width of the sample, as the wedge is wider than the sample. From studies on the emitted wave field of a wedge-transducer generation string, it can be assumed that this pairing averages the amplitudes approximately with a Gaussian shaped filter.

Table (6.1) sums up the fundamental characteristics of the two measurement methods.

Table 6.1: Comparison between air-coupled and wedge detection

Characteristic	Air-Coupled	Wedge
Calibration needed	Yes	No
Measurement Period	$0.5h$	$2.5h$
Datapoints per Measurement	24	11
2D-scan possible	Yes	No
Signal-to-Noise ratio	low	high
Area of Averaging	rather small	rather large
Averaging Filter	Unknown	Gaussian

Figures (6.1) and (6.3) show exemplary results for air-coupled and wedge detection of the fundamental (top) and second harmonic (bottom) amplitudes and figures (6.2) and (6.4) the calculated ratio $\frac{A_2}{A_1^2}$ over the propagation distance for the two measurement methods applied on the fabricated samples.

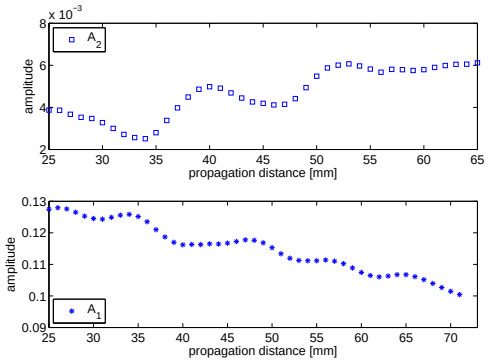

Figure 6.1: Amplitudes over propagation distance (air-coupled)

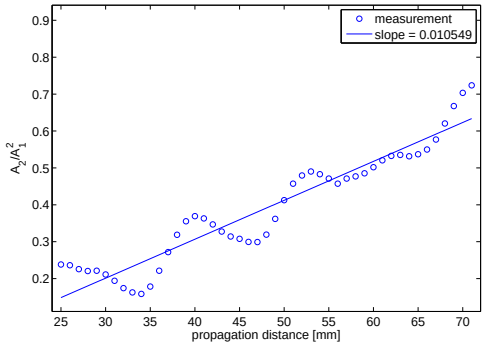

Figure 6.2: Ratio over propagation distance (air-coupled)

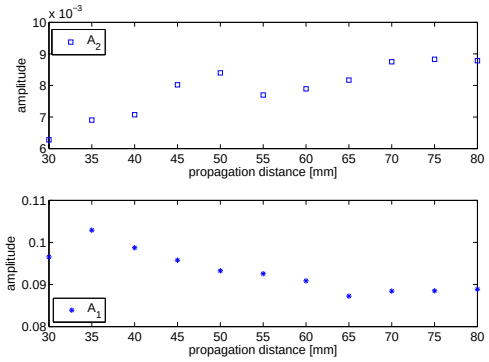

Figure 6.3: Amplitudes over propagation distance (wedge)

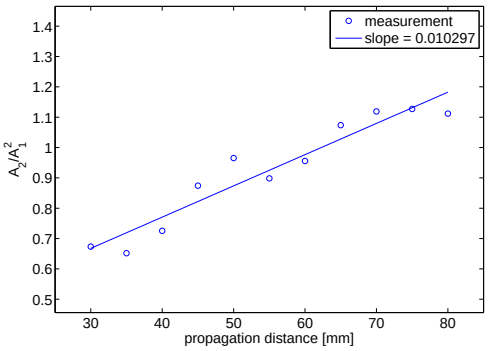

Figure 6.4: Ratio over propagation distance (wedge)

Due to the fast non-contact measurement, the air-coupled measurement provides much more datapoints than the wedge detection method in less measurement time. However, it is obvious that the slope of the ratio $\frac{A_2}{A_1^2}$ over the propagation distance x

is hard to evaluate as there is some kind of oscillating characteristic in the obtained result. Therefore, the measured relative nonlinearity parameter β' has a dramatic variation and it is not possible to obtain consistent results out of several measurements.

A similar effect in a much softer form can be observed for the wedge-detection. Fortunately, the wedge detection method proved to have only slight variation in the measured β' which makes this method suitable for the detection in the conducted experiments.

The oscillating characteristic has been previously observed in various researches using non-contact detection, e.g. by Blackshire et al. with laser detection [4]. According to this work, the oscillating effect is originating from side reflections of the propagating SAW. In addition to that, the leaking of P-waves into the air in the edge region of the sample might be a very complex mechanism that further adulterates the air-coupled measurements.

To get a better impression of these oscillating effects, the fundamental wave field is examined more precisely performing a 2D scan using laser detection. Figure (6.5) shows the results of the 2D laser scan.

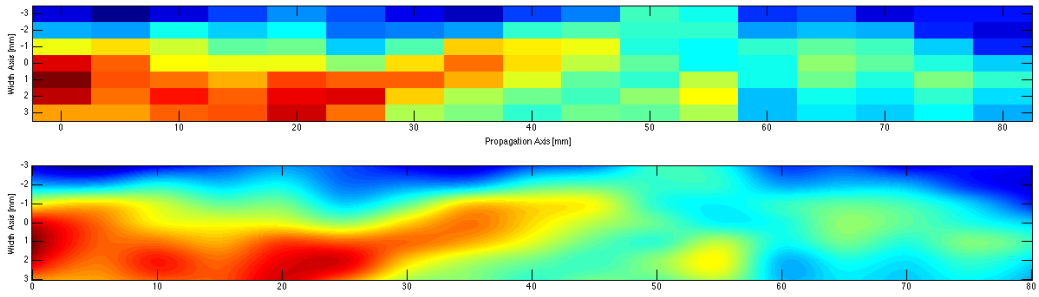

Figure 6.5: 2D scan obtained with laser detection (top) and interpolated image (bottom)

The top shows the actual obtained data from the laser and the lower picture shows

an interpolation of this data. Apparently, the wave beam seems to get reflected several times from the sample's edge within the range of the conducted measurements. This also explains, why preliminary air-coupled measurements conducted on the uncut base material plate did not show the oscillating behavior depicted in figure (6.1). These observations prove that edge effects are the cause for the poor results of the air-coupled transducer for the fabricated samples.

Positively, for the wedge-detection method might be, that the wedge-transducer combination gathers and averages the displacement over the whole sample width. Its output is a weighted average of displacement over the whole sample width, and therefore a measure of the energy of the propagating wave. Thus, the observed side reflections have "less impact" on the measured amplitudes.

On the other hand, the air-coupled transducer averages over a smaller area and therefore, a much more localized value of the displacement is obtained. Furthermore, the leaking of acoustic waves in the air is a complex mechanism in these edge regions and not fully understood yet. Conclusively, this leads to a drastic impact of side effects on the measurement results.

The sole and exclusive remedy for the occurring measurement problems caused by edge effects is found in increasing the sample width. However, as mentioned in chapter (4) the cross section of the produced samples is defined by the maximum applicable load. As this load needs to be slightly above yield strength, a further increase in sample width is not possible.

Summarizing this, one might favor air-coupled detection with respect to time consumption but in the case of limited sample width (as it is the case in this research), air-coupled detection is not suitable and leads to poor results. Thus, wedge detection is chosen to investigate the relationship between the relative nonlinearity parameter β' and the level of SCC damage induced in the material.

6.2 Preliminary Measurements on a Welded Plate

Despite the choice of a measurement method, a second goal of these preliminary results is to investigate the impact of actual welding regions on nonlinear Rayleigh wave measurements. As described in chapter (3), the microstructural changes affecting the material's susceptibility to SCC are occurring in the HAZ of a weld. Hence, a change in material nonlinearity due to an increasing degree of SCC damage is expected to be observable in this region.

For the samples used in this research, this HAZ of a weld is "simulated" by sensitization in order to obtain a sufficiently large region to perform nonlinear Rayleigh measurements in it. However, in addition to the sensitized samples a welded plate was fabricated to estimate the impact of welded areas on the propagation of Rayleigh surface waves. Therefore, a 2D-scan of the fundamental and the second harmonic amplitudes of the wave field is conducted using air-coupled detection. Since a plate is used for these measurements, air-coupled detection is perfectly suitable and there are no edge effects impeding the measurements. The measurement is performed as a "cross-weld" measurement as it is depicted in chapter (4) in figure (4.2). The generating wedge is joined to the sample in such way, that the weld material starts at a propagation distance of approximately $60-65mm$. Figures (6.6) and (6.7) present the normalized fundamental and second harmonic amplitudes of an area close to the weld.

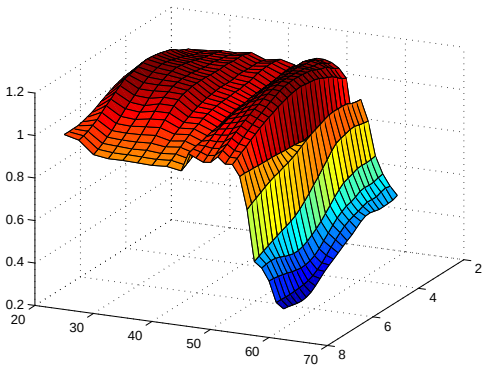

Figure 6.6: 2D-scan of fundamental amplitude near weld

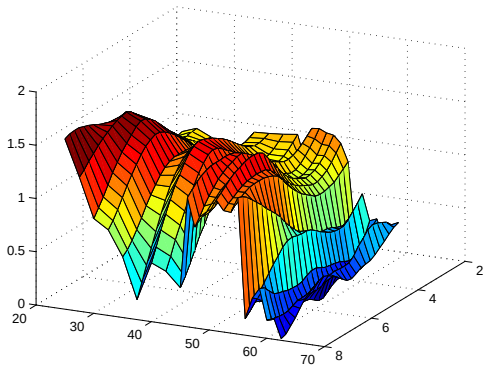

Figure 6.7: 2D-scan of second harmonic amplitude near weld

The results clearly display a harsh drop in both, fundamental and second harmonic amplitude in the welded area. One could argue that this drop is caused by a change in surface quality in the welded area and with to this related leaking differences of acoustic waves into the air. However, further cross-weld measurements during which the generating wedge is joined closer to the welded area and the air-coupled detected the wave field on the other side of the weld reveal that the measured amplitudes after crossing the weld are less than 10% of the amplitudes measured before crossing the weld. In comparison, without crossing a weld, the amplitudes typically drop to values of $70-80\%$ over the examined propagation distance. This dramatic distortion of Rayleigh surface waves in welded areas makes so called cross-weld measurements very difficult.

CHAPTER VII

TRACKING SCC WITH NONLINEAR RAYLEIGH WAVES

This chapter presents and interprets nonlinear Rayleigh wave measurement results from samples with different degrees of stress corrosion damage. These nonlinear ultrasonic Rayleigh measurements are supported by a complementary microscopic examination of the samples.

7.1 Nonlinear Rayleigh Wave Measurement Results

The results presented in this section are obtained using wedge detection. The measurement procedure for this is described in detail in chapter (5).

As already stated, measurements are performed for two different applied loads during the SCC setup - one set of samples is loaded with 105% and one with 110% of yield strength. For each set, samples with one, three and five weeks of holding time in the SCC cell are fabricated. On top of that, nonlinear Rayleigh wave measurements are performed on baseline samples, that are neither sensitized, nor corroded and on sensitized but non-corroded samples to obtain a baseline and to estimate the impact of sensitization on the nonlinearity parameter. Four to eight measurements are performed for each sample. All of this section's figures will depict normalized mean values of these four to eight measurements and the corresponding error bars.

Figures (7.1) and (7.2) show the trend in the relative nonlinearity parameter β' for the two different load levels over SCC holding time. The results are normalized over the mean value of the baseline nonlinearity parameter. Furthermore, values for the

sensitized samples are included in these figures.

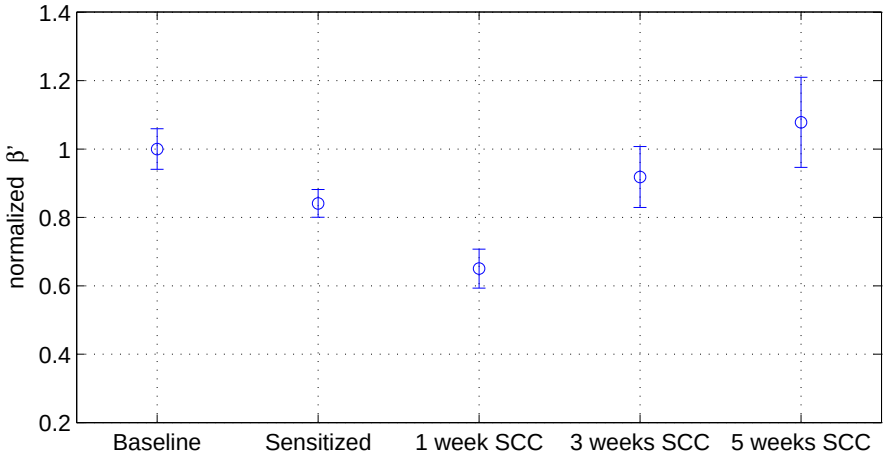

Figure 7.1: Normalized β' over SCC holding time for 105% YS applied load

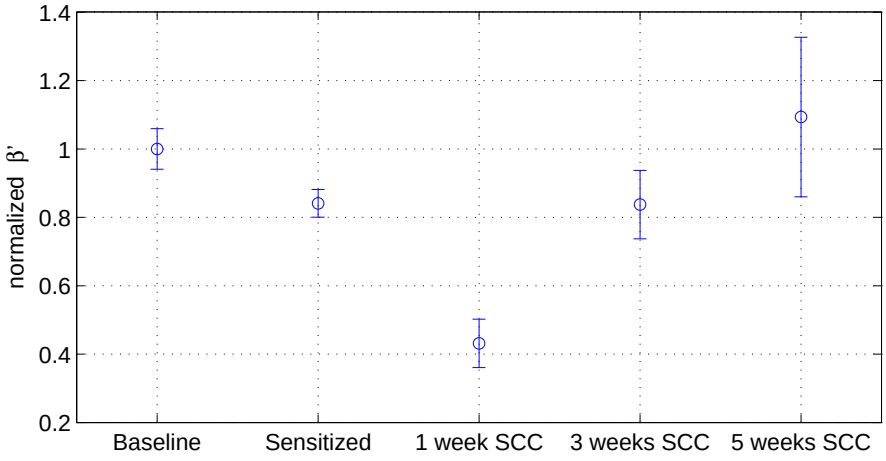

Figure 7.2: Normalized β' over SCC holding time for 110% YS applied load

A first observation one can draw, is that the relative nonlinearity parameter decreases by approximately 15% due to sensitization. As already stated in chapter (3) various counteractive processes are happening during sensitization. The formation of

chromium carbides at the grain boundaries has proven to increase the relative nonlinearity parameter. However in this case, the effect of these precipitates is eclipsed by dislocation movement and annihilation which is, on the contrary, known to decrease material nonlinearity. This makes perfect sense in the way, that the base material for this research is a cold-rolled stainless steel plate and cold work is known to induce a high amount of dislocations density in the material. While heating the material, the movement and creeping of these dislocations is facilitated which leads to a partial annihilation. Hence, the heat treatment for sensitization decreases dislocation density and, therefore, also the material nonlinearity.

A second observation one can make is that β' further decreases during the first week of SCC although the formation of microcracks during SCC is known to increase the material nonlinearity. A discussion of this trend will occur later in this section.

Lastly, one can observe an increase in the relative nonlinearity parameter after more than one week of SCC holding time. This trend can be explained by the formation and growth of microcracks. As explained in detail in chapter (3), microcracks are introduced in the material during SCC. These cracks cause a clapping nonlinearity that generates higher harmonics of a propagating wave. Therefore, the relative nonlinearity parameter β' is sensitive to these cracks and increases with increasing number and size of cracks. The longer the samples are held in the SCC cell, the greater β' will become as more cracks are initiated and already initiated cracks grow larger.

So far, the results obtained are perfectly conclusive and as expected with one exception - the further drop in β' during the first week of SCC has still to be explained. The surrounding media during SCC is held at room temperature, therefore, no temperature caused creeping of dislocations can occur. However, dislocation movement and annihilation is also facilitated by applied stress.

In order to investigate the further drop in β' during the first week of SCC, a sensitized sample is loaded with 110% YS for one week without corrosive environment. As

all parameters excluding the surrounding medium are held constant, a comparable trend in measured material nonlinearity should be observable for this sample as it was seen for the one week corroded samples, if stress caused creeping of dislocations is the reason for the drop in β'. Figure (7.3) shows the change in measured material nonlinearity caused by the loading of the sample solely, again normalized over the mean value of the baseline nonlinearity parameter.

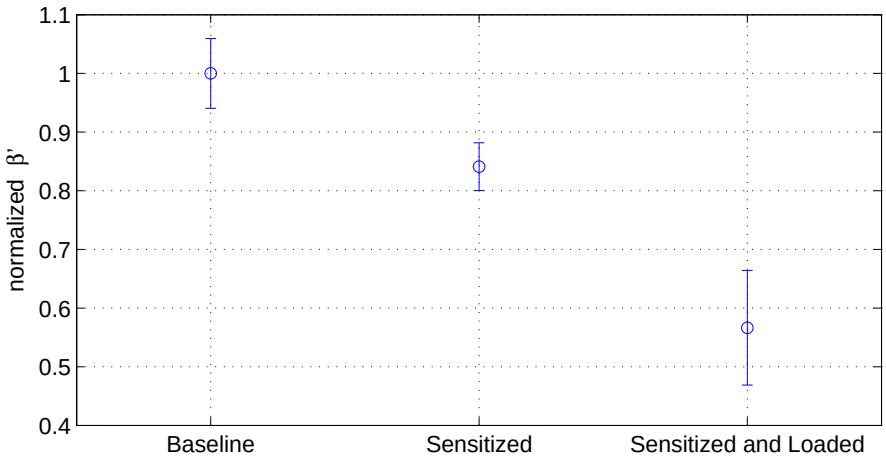

Figure 7.3: Trend in normalized β' for sensitization and loading at 110% YS for one week

This figure clearly shows a further drop in the relative nonlinearity parameter β' of approximately 30% as it is loaded with 110% YS for one week. This proves the assumption that there is a significant amount of dislocations left in the material after sensitization, and that these dislocations move and annihilate during the first week of applied load.

Figure (7.4) combines figures (7.1) and (7.2) adding the newly obtained data for the sensitized and loaded sample. The measured β' is normalized over the nonlinearity parameter of the baseline sample.

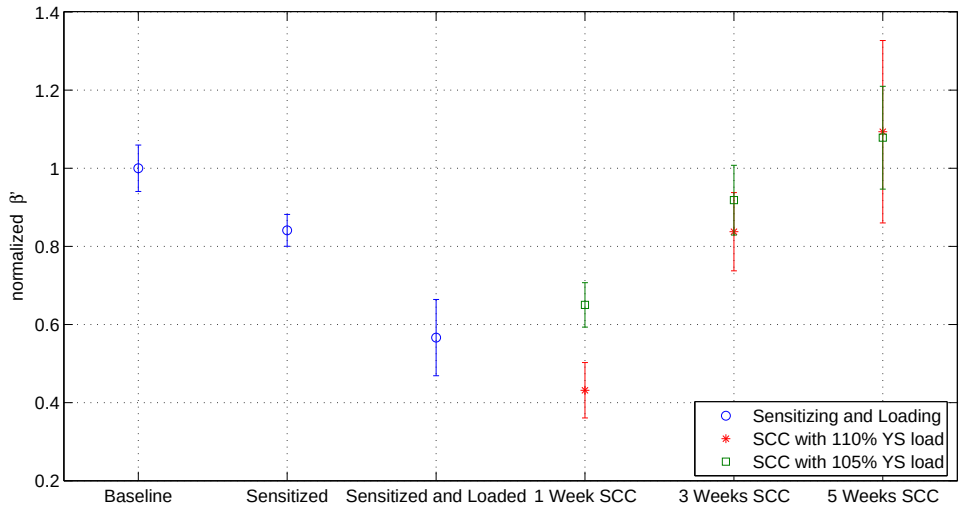

Figure 7.4: Trend in normalized β' for sensitization, loading and SCC

This figure shows that the drop in measured material nonlinearity for the one week loaded sample without the presence of the corrosive environment is of the same magnitude as the drops for the two samples with one week of SCC. It has been shown, that stress caused creep of dislocations induces a drop in material nonlinearity during the first week of SCC. The microscopic analysis presented in the next section additionally indicates that no significant number of microcracks is initiated during this period. Thus, the phenomenon of this drop in material nonlinearity is explained and attributed to the further annihilation of dislocations.

Figure (7.5) helps to directly compare the trends in measured material nonlinearity for the two loading levels. The values are normalized over the parameters of the samples corroded for one week, as material nonlinearity seems to take on a minimum value for approximately one week of SCC. Although the measurements on the most corroded sample (5 weeks of SCC at 110% YS) yield an unusual big error bar, one can clearly see an increasing trend in the measured material nonlinearity for both sample sets. Furthermore, it is obvious that the relative nonlinearity parameter β' increases by a higher rate for the higher loaded samples. Similar observations were made by

Zeitvogel [25].

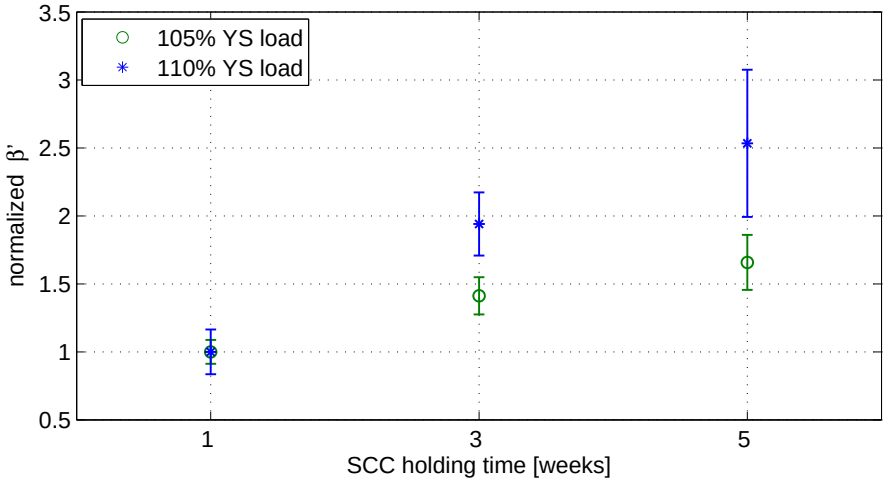

Figure 7.5: Trend in normalized β' over SCC holding time for 105% and 110% YS applied load

7.2 Microscopic Analysis of the Sample Surface

Some exemplary microscopic pictures of the sample surfaces are presented. These pictures shall underline the validity of the results obtained from the nonlinear Rayleigh measurements. Although, there is no extensive quantitative microscopic crack analysis conducted on the samples, one can draw conclusions from random microscopic inspection of the sample surface. This random microscopic inspection shall only help to explain the obtained trend in the relative nonlinearity parameter β'.

Before microscopy, the samples were once again polished with 800 grid sandpaper. For this grinding process, it is important to remove the top layer only - the passive oxide layer - instead of abrading too much. Else smaller microcracks would be grind off completely and not be visible anymore. Furthermore, it is important to polish the surface of each sample to the same extend, to not adulterate any results by removal of smaller microcracks.

Once the samples are polished, they are examined under 100x, 500x and 1000x zoom. Stress corrosion cracks are hard to detect under 100x zoom, and might only be visible using a higher magnification. However, the 100x zoom might give an expression on the amount of cracks in a specific surface area.

Figures (7.6) to (7.8) show exemplary microscopic pictures of a non-corroded sample. Obviously, one can not discover any microcracks during examination of the sample surface.

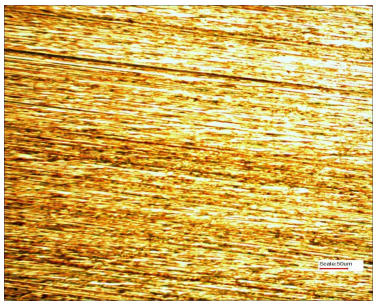

Figure 7.6: Microcopic picture of baseline sample with 100x zoom

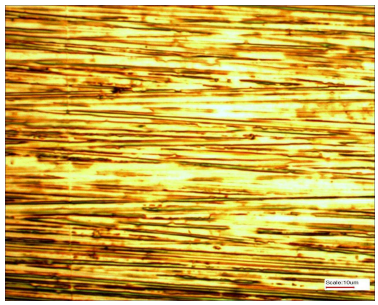

Figure 7.7: Microcopic picture of baseline sample with 500x zoom

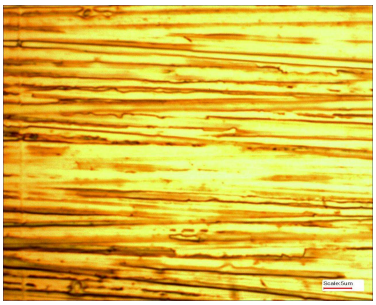

Figure 7.8: Microcopic picture of baseline sample with 1000x zoom

One Week of SCC

Microscopic analysis of the two samples that are held for one week in the SCC cell does not reveal any microcracks. Even under 1000x magnification, there are no visible cracks observed, i.e. the microscopic pictures taken are similar to the ones shown above (figures (7.6) to (7.8)). As discussed earlier, there is no large-scale quantitative microscopic analysis conducted but instead the samples are only randomly inspected at numerous locations. Thus, not discovering any microcracks does not necessarily imply that there are no microcracks. However, one can conclude that there is no significant crack density on the surface and therefore, one can expect the change in material nonlinearity due to SCC to be relatively low. This underlines that the drop

in measured material nonlinearity is caused by dislocation movement and annihilation due to applied stress and that there is no significant clapping nonlinearity increasing β' as there is no significant amount of microcracks initiated yet.

Three Weeks of SCC

Figures (7.9) and (7.10) show microscopic images of the sample corroded for three weeks with a load of 105% YS. Similarly, figures (7.11) and (7.12) show images for the sample loaded with 110% YS.

The blue ellipses in the 100x magnified images indicate SCC features. The 1000x magnified image shows a close-up view of a stress corrosion crack. Random inspection of these two samples reveals numerous microcracks for both samples. However, the crack density of the inspected sample surfaces can still be considered relatively low.

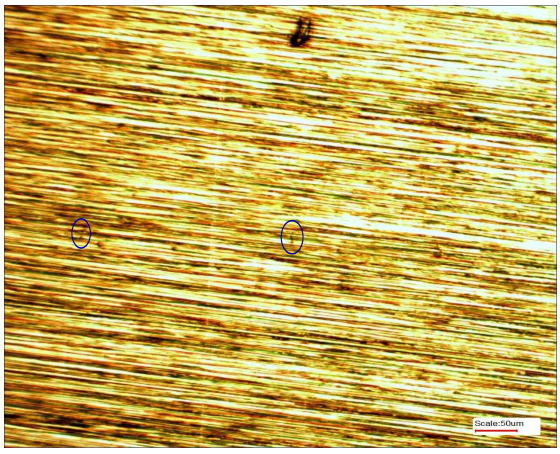

Figure 7.9: Microcopic picture with 100x zoom of sample corroded for three weeks with 105% YS applied load

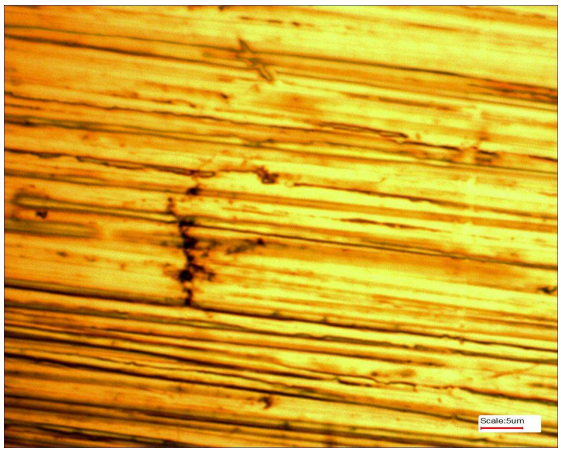

Figure 7.10: Microcopic picture with 1000x zoom of sample corroded for three weeks with 105% YS applied load

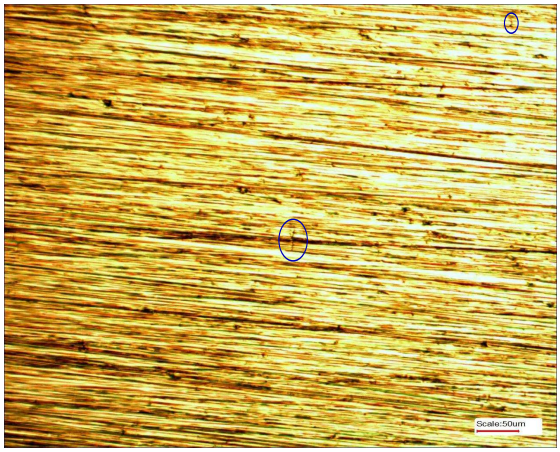

Figure 7.11: Microcopic picture with 100x zoom of sample corroded for three weeks with 110% YS applied load

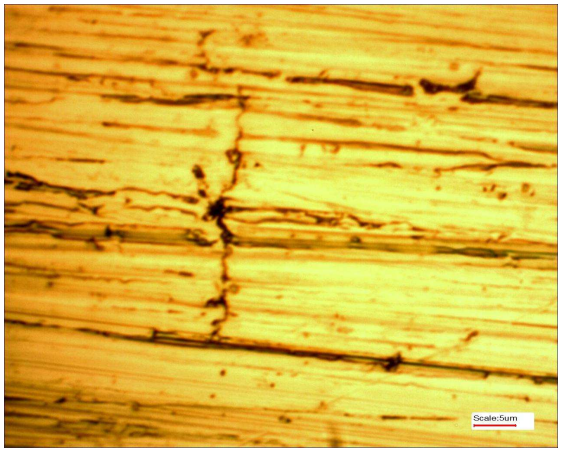

Figure 7.12: Microcopic picture with 1000x zoom of sample corroded for three weeks with 110% YS applied load

Five Weeks of SCC

Microscopic images for the two samples corroded for five weeks are shown in the figures (7.13) to (7.16). Once again, the blue ellipses in the 100x magnified images indicate SCC features and the 1000x magnified images show close-up views of an exemplary stress corrosion crack. One can easily notice that the density of stress corrosion cracks increases significantly from the third to the fifth week of SCC. Furthermore, not only smaller, but also bigger microcracks can be observed for this level of SCC damage. The microscopic images also reveal a difference in SCC damage for the two load levels - the sample loaded with 110% YS apparently seems more corroded than the sample corroded with a lower applied load.

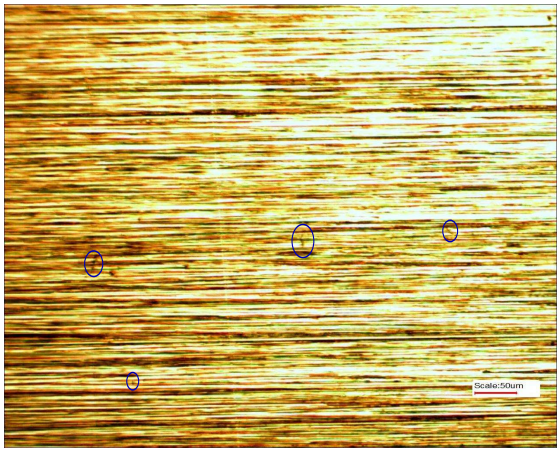

Figure 7.13: Microcopic picture with 100x zoom of sample corroded for five weeks with 105% YS applied load

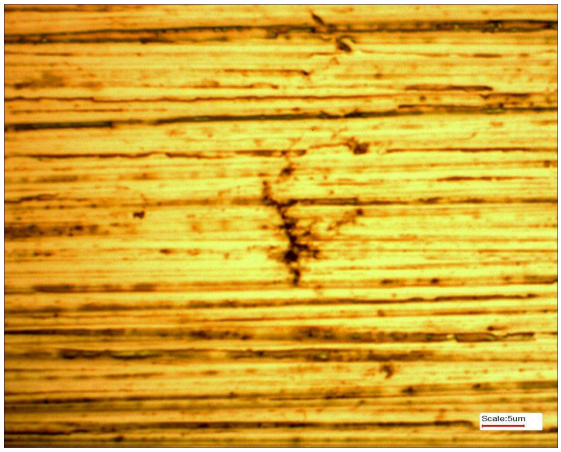

Figure 7.14: Microcopic picture with 1000x zoom of sample corroded for five weeks with 105% YS applied load

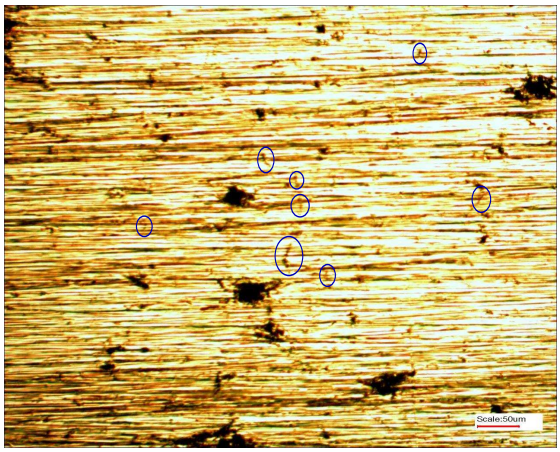

Figure 7.15: Microcopic picture with 100x zoom of sample corroded for five weeks with 110% YS applied load

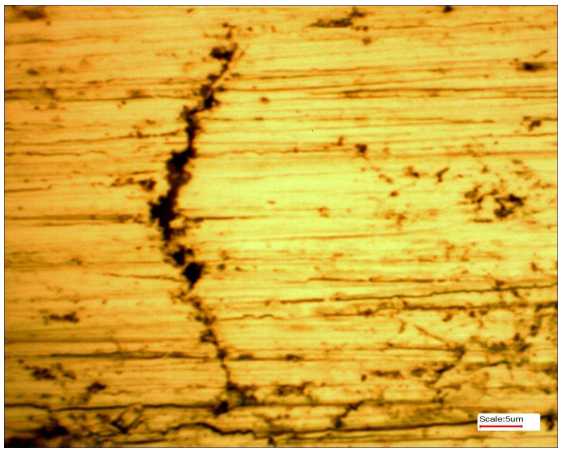

Figure 7.16: Microcopic picture with 1000x zoom of sample corroded for five weeks with 110% YS applied load

CHAPTER VIII

CONCLUSION AND OUTLOOK

This final chapter summarizes the results obtained, giving a brief conclusion of this work. Additionally, an outlook is given on possible future work in this area of research.

8.1 Conclusion

This research develops a robust method to measure material nonlinearity in sensitized 304 stainless steel. The second harmonic generation for Rayleigh surface waves is investigated using wedge detection for increasing propagation distances. In the early chapters of this work, the theoretical background for the generation of the second harmonic wave and the nonlinear propagation of Rayleigh surface waves is presented. Likewise, the microstructural changes caused by sensitization and SCC of the material are described and related to a change in material nonlinearity. Two different approaches are described, applied and compared before the wedge detection method with varying propagation distance is chosen.

From a nondestructive evaluative point of view, this method reveals an interesting trend for the relative nonlinearity parameter, β'. This parameter is measured in samples with different levels of SCC damage. It is shown, that the high dislocation density in cold rolled 304 SS causes an initial, very high material nonlinearity. During the sensitization process and the early stages of SCC, i.e. the first week of SCC, the dominant process affecting material nonlinearity is found to be dislocation movement and annihilation which results in a decrease in the measured β'. Microscopy on these samples reveals that there is not a significant amount of microcracks introduced into the material during the first week of SCC.

Further introduction of SCC damage, in particular longer holding times in the SCC cell, initiates microcracks and subsequently the growth of initiated microcracks for longer times. After three and five weeks of holding time in the SCC cell, random microscopic inspection displays a large number of stress corrosion cracks on the sample surface. For these samples, the nonlinear Rayleigh wave measurements show an increasing trend in the measured relative nonlinearity parameter for increasing holding times. Thus, it is shown that it is possible to relate the material nonlinearity to the degree of SCC damage induced in the material which is the main goal of this research. Although this research focuses on examining sensitized 304 SS specimens, similar results can theoretically be obtained using actual welded samples. The sensitization process simply "simulates" a HAZ. This means the microstructural changes that occur in the HAZ during a welding process are evoked within the whole sample during sensitization. This is beneficial for the proposed measurement method, as nonlinear surface wave measurements require a large area. Theoretically, one could conduct the same measurements on an actual weld and one should be able to observe similar changes in material nonlinearity. However, the HAZ of this theoretical weld has to be sufficiently large.

8.2 Outlook

This work shows the feasibility of detecting SCC damage in 304 stainless steel using nonlinear ultrasound, i.e. nonlinear Rayleigh wave propagation. In particular, the early stage of SCC damage is the focus of this research. Hence, a relatively low degree of SCC damage is introduced in the material. From a material point of view, it would be interesting to extend these measurements until the point where macrocracks are formed. At this point, the second harmonic amplitude will be strongly attenuated and the relative nonlinearity parameter β' will decrease again. Furthermore, this is also

the point where linear ultrasonic methods will become sensitive to the SCC damage induced in the material.

Additionally, it would be interesting to quantify these results and to quantitatively relate the induced SCC damage to the change in the nonlinearity parameter β'. For these purposes, it is essential to eliminate coexistent processes that affect the material nonlinearity, for example the movement and annihilation of dislocations, at its best. Therefore, the material should be annealed before sensitization.

Furthermore, to prove the hypothesis on high dislocation density due to cold work and the drop in material nonlinearity due to dislocation annihilation, transmission electron microscopy (TEM) could be performed on the samples used in this research.

Another interesting area of research for future work would be the application to actual welded samples. As shown in chapter (6), there exist difficulties in applying nonlinear ultrasonic methods using surface waves on welded samples. The measurements performed on welded samples in this research revealed a drastic scattering and attenuation of the wavefield while passing the welded area. However, this could also be caused by poor welding or surface conditions.

Last but not least, it is crucial to identify the source for the poor results using air-coupled detection in this research. The air-coupled detection provides a method to scan more measurement points in less time. However, to successfully benefit from the advantages of this non-contact detection method, one has to be fully aware of its spatial averaging characteristic and the impact of sample geometry on the measurement results. Therefore, an appealing topic for future research would be to determine the exact averaging characteristic of the air-coupled transducer and its limits regarding measurements on samples of finite width.

REFERENCES

[1] Abraham, S., "Assessment of sensitization in aisi 304 stainless steel by nonlinear ultrasonic method," *Acta Metallurgica Sinica*, vol. 26, pp. pp. 545–552, 2013.

[2] Aschenbach, J., *Wave propagation in elastic solids*. North-Holland, 1999.

[3] Assis, J., "X-ray analysis of residual stress distribution in weld region," *Advances in X-Ray Analysis*, vol. 45, pp. pp. 225–231, 2002.

[4] Blackshire, J., "Nonlinear laser ultrasonic measurement of localized fatigue damage," *Review of Quantitative Nondestructive Evaluation*, vol. 22, 2003.

[5] Cantrell, J. and Yost, W., "Nonlinear ultrasonic characterization of fatigue microstructures," *International Journal of Fatigue*, vol. 23, no. No. 1, pp. pp.487–490, 2001.

[6] Caseres, L. and Mintz, T., "Atmospheric stress corrosion cracking susceptibility of welded and unwelded 304, 304l, and 316l austenitic stainless steels commonly used for dry cask storage containers exposed to marine environments," *Office of Nuclear Regulatory Research U.S. Nuclear Regulatory Commission*, 2010.

[7] Chen, Y., "Thermodynamically modeling the interactions of hydrogen, stress and anodic dissolution at crack-tip during near-neutral ph scc in pipelines," *Journal of Materials Science*, vol. 42, no. No. 8, pp. pp. 2701–2705, 2007.

[8] Cragnolino, G. and Macdonald, D., "Intergranular stress corrosion cracking of austenitic stainless steel at temperatures below 100 c a review," *Corrosion*, vol. 38, no. No. 8, pp. pp. 406–424, 1982.

[9] DerrinFreshWaterInstitute, "Retrieved from: http://www.rpi.edu/dept/dfwi/facilities/keck/instrumentation.html," Keck Water Research Laboratory (July 2014).

[10] Graff, K., *Wave motion in elastic solids*. New York: Dover Publications, 1991.

[11] Green, A., "A general theory of an elastic-plastic continuum," *Archive for Rational Mechanics and Analysis*, vol. 18, p. pp. 251, 1965.

[12] Hamilton, M. and Blackstock, D., *Nonlinear Acoustics*. Academic Press, 1998.

[13] Herrmann, J., "Assessment of material damage in a nickel-base superalloy using nonlinear rayleigh surface waves," *Journal of Applied Physics*, vol. 99, 2006.

[14] Kim, J.-Y. and Jacobs, L., "Experimental characterization of fatigue damage in a nickel-base superalloy using nonlinear ultrasonic waves," *The Journal of the Acoustical Society of America*, vol. 120, p. pp. 1266, 2006.

[15] Liu, M., "Experimental study of nonlinear rayleigh wave propagation in shot-peened aluminum platesfeasibility of measuring residual stress," *NDT AND E International*, vol. 44, no. No. 1, pp. pp. 67–74, 2011.

[16] Matlack, K., Kim, J.-Y., Jacobs, L., Qu, J., and Singh, P., "Nonlinear rayleigh waves to detect initial damage leading to stress corrosion cracking in carbon steel," *AIP Conference Proceedings*, vol. 1430, no. No. 1, p. pp.1452, 2012.

[17] MetallurgicalTechnologies, "Retrieved from: http://www.met-tech.com/metallography.html," *Metallurgical Technologies, Inc.*, (July 2014).

[18] Newman, R., Sieradzki, K., and Isaacs, H., "Stress-corrosion cracking of sensitized type 304 stainless steel in thiosulfate solutions," *Metallurgical Transactions A*, vol. 13, no. No. 11, pp. pp.2015–2026, 1982.

[19] Norris, A., "Symmetry conditions for third order elastic moduli and implications in nonlinear wave theory," *Journal of Elasticity*, vol. 25, pp. pp. 247–257, 1991.

[20] Rose, J., *Ultrasonic waves in solid media*. UK: Cambridge University Press, 1999.

[21] Staehle, R., "Stress corrosion cracking (and corrosion fatigue)," *Materials Science and Engineering*, vol. 25, pp. pp. 207–215, 1976.

[22] Thiele, S., *Air-coupled Detection of Rayleigh Surface Waves to Assess Material Nonlinearity due to Precipitation in Alloy Steel*. Master's Thesis, Georgia Institute of Technology, 2012.

[23] Viktorov, I., *Rayleigh and Lamb waves: physical theory and applications*. New York: Plenum Press, 1967.

[24] Viswanath, A., "Microstructural characterization of m250 grade maraging steel using nonlinear ultrasonic technique," *Journal of Materials Science*, vol. 45, no. No. 24, p. pp. 6719, 2010.

[25] Zeitvogel, D., "Characterization of stress corrosion cracking in carbon steel using nonlinear rayleigh surface waves," *NDT AND E International*, vol. 62, pp. pp.144–152, 2014.